Featured in Physics

Simple Reaction-Diffusion Modeling Predicts Inconspicuous Neighborhood-Dependent Color Subclustering of Lizard Scales

Szabolcs Zakany* and Michel C. Milinkovitch†

Laboratory of Artificial and Natural Evolution (LANE), Department of Genetics and Evolution, University of Geneva, 1211 Geneva, Switzerland and SIB Swiss Institute of Bioinformatics, 1211 Geneva, Switzerland

(Received 9 June 2023; accepted 1 September 2023; published 20 October 2023)

Turing proposed a reaction-diffusion (RD) process as the chemical basis of morphogenesis. Despite the elegance of this model, its relevance for the precise description of morphogenesis in real organisms is largely disputed. Here, we show that a simple RD system, predicting the cellular-automaton-like patterning of ocellated lizards' skin into green and black labyrinthine chains of scales, additionally predicts unsuspected subtle color subclustering that correlates with the colors of the scales' neighbors. Hyperspectral imaging indicates that color subclustering is present in real lizards, confirming the numerical model nontrivial prediction. In addition, extensive histological analyses show that melanophores' spatial distribution correlates with scale neighborhood, confirming that color subclustering is associated to the underlying microscopic system of chromatophore interactions. We then show that the observed subclustering is efficiently captured by RD models, irrespective of their form, discretization, and spatial dimensionality. We also show that sets of values can be identified in the 12-dimensional RD parameter space to yield the correct direction of correlation (i.e., observed in real lizards) between green-scale blackness and their neighborhood configuration, hence instructing the mathematical model. More generally, our results show that subtle mesoscopic properties of biological dynamical systems, as well as some of the underlying microscopic features, are quantitatively captured by simple RD models without integrating the unmanageable profusion of variables at lower scales.

DOI: 10.1103/PhysRevX.13.041011 Subject Areas: Biological Physics, Statistical Physics

I. INTRODUCTION

In his classic 1952 article [1], Turing used nonlinear partial differential equations describing a system of reacting and diffusing components [accordingly, the model is typically called "reaction-diffusion" (RD)] that can generate a wide range of spatiotemporal dynamics [2] (chaotic, nearly chaotic, cyclic, solitonic) of components' concentrations, but also stationary symmetry-breaking patterns such as spots, stripes, and labyrinths. Turing focused on stationary patterns and proposed that RD constitutes the chemical basis of morphogenesis; hence, the term "morphogen" that he introduced [1] to describe RD components. Although the elegance of Turing's model and its enormous significance in the field of nonlinear dynamics have been universally praised [3–7], much debate is still ongoing about the relevance of RD for describing actual morphogenesis in real biological systems, especially against an alternative, but not mutually exclusive [8], model of morphogen gradient-dependent positional information [9–11].

Because (i) skin color patterns in vertebrates emerge during development through spatial segregation of chromatophores (i.e., cells producing pigmentary or structural colors [12–16]) and (ii) this process is driven by interactions among chromatophores [Fig. 1(a)] that consist of activations and inhibitions [17–22] established through short- and long-range cell-cell contacts [21,23], it has been suggested [5,6,17,24,25] that the resulting self-organizational dynamical system can be quantitatively investigated at the continuum limit as a RD model with effective slow- and fast-diffusing components. In addition, we have recently identified [24,25] that the phenomenon of color switching (green to black and black to green) of individual skin scales during the posthatching development of ocellated lizards (*Timon lepidus*) is emerging from the superposition of such a system of RD equations with the 3D geometry of the lizard skin. Indeed, reduction of diffusion at the thin borders of much thicker scales not only causes

*szabolcs.zakany@unige.ch

†Author to whom correspondence should be addressed: michel.milinkovitch@unige.ch

Published by the American Physical Society under the terms of the Creative Commons Attribution 4.0 International license. Further distribution of this work must maintain attribution to the author(s) and the published article's title, journal citation, and DOI.

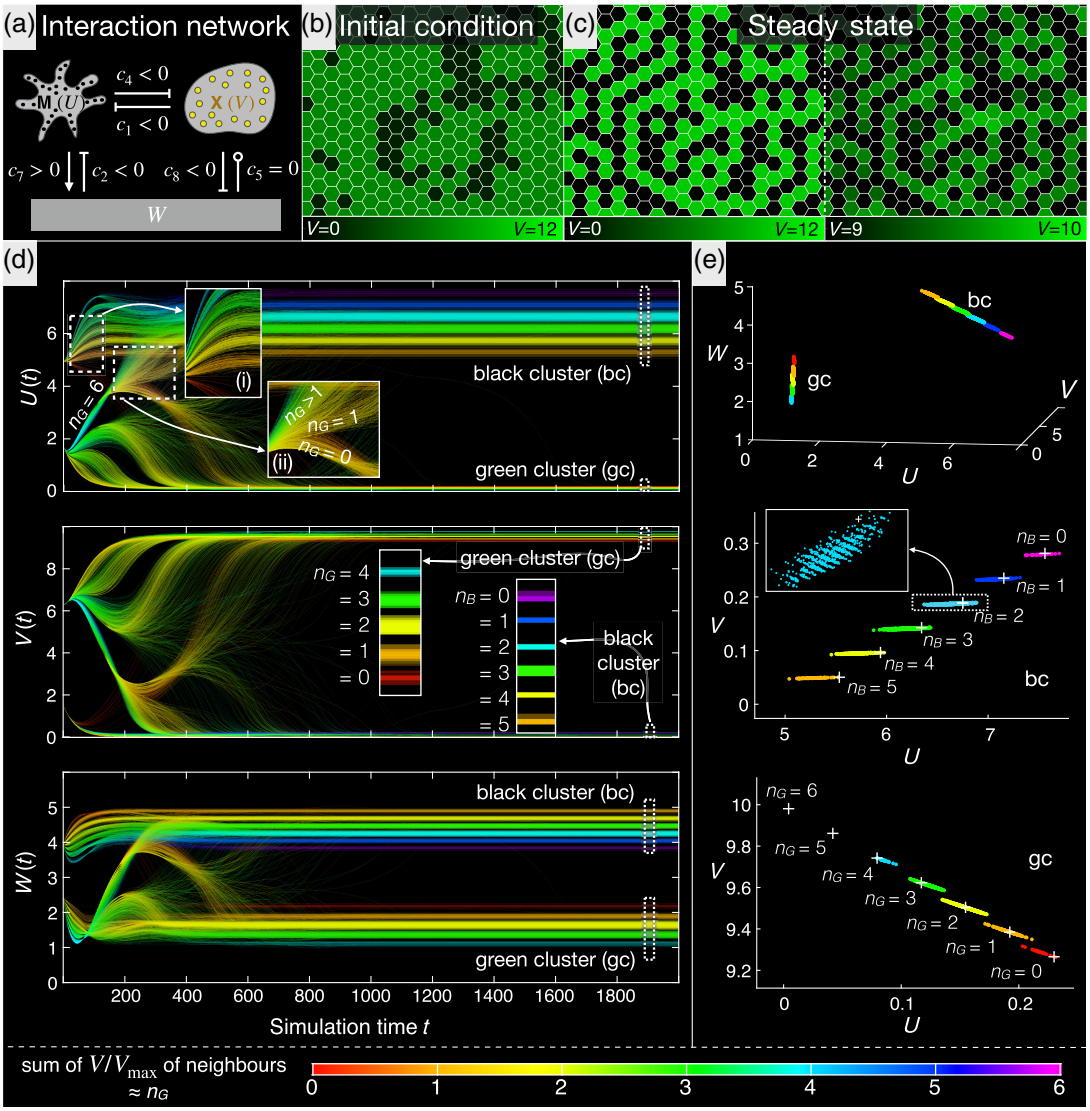


FIG. 1. Discrete reaction-diffusion (dRD) simulations indicate neighborhood-dependent scale color subclustering. (a) Signs of interactions between chromatophores [17]; short-range compounds U and V represent melanophores (M) and xanthophores (X) in the dRD model; W is the long-range factor. (b),(c) Enlarged detail of a lattice of 3850 hexagons with (b) juvenilelike initial condition and (c) steady-state pattern [$t > 1800$; levels of green indicate unnormalized (left) and normalized (right) values of V]. (d) Heat maps: evolution of densities U (top), V (middle), and W (bottom) for all hexagons. Subclustering of (U, V, W) is apparent at late times in both the green and black clusters. Dynamical "lineages" of time evolution are visible at earlier times [insets (i) and (ii)]. Time trajectory of each hexagon is dynamically colored according to its nearest-neighbor configuration (bottom panel, $V_{max} = 10$). (e) Clustering and subclustering of (U, V, W) of all hexagons at steady state ($t > 1800$); values subcluster according to the number of black (n_B) or green (n_G) nearest neighbors. Coloring of data points as in (d). Top: green cluster (gc, $U < 2.5$, $V > 4.5$) and black cluster (bc, $U \geq 2.5$, $V \leq 4.5$); the 3D graph is provided as Supplemental Material, File S1 [34]. Middle: enlargement of the black cluster in (U, V) projection; inset illustrates subsubclustering (for $n_B = 2$). Bottom: enlargement of the green cluster in (U, V) projection. White crosses indicate analytical approximation of steady-state subcluster locations (see Appendix A 2).

the RD pattern to "snap" with the lattice of scales (hence, making each scale monochromatic [24]) but also effectively [24] and robustly [25] transforms the skin color patterning process into a mesoscopic stochastic cellular automaton [26–29] (sCA) that dynamically computes the late-time steady-state labyrinthine pattern of green and black chains of scales observed in real lizards. In addition, we have shown [30] that the patterning dynamics and late-time probability distribution of patterns in real ocellated lizards can be efficiently described by the canonical probability distribution of the simpler antiferromagnetic two-parameter Lenz-Ising model [31,32]. Finally, we have shown that, although all three models efficiently predict neighborhood statistics of very different adult patterns exhibited by five divergent species of lizards, RD predicts individual scale-by-scale patterns, i.e., the exact position of green or yellow

and black scales, substantially better than Lenz-Ising and CA models [33].

In an attempt to bridge the gap between, on one hand, time- and space-discretized statistical models (sCA and Lenz-Ising) and, on the other hand, the RD framework, we formally derived [24] on the hexagonal 2D lattice a discrete RD (dRD) model from Turing's continuous RD equations by renormalizing the diffusion term. Besides capturing the scale-by-scale sCA or Lenz-Ising color-switching dynamics, the dRD model keeps the complexity of two important (linked) variables of the underlying continuous RD (cRD) model: continuous state and continuous time dynamics (both discrete in the sCA and Lenz-Ising). Indeed, scales can, in principle, take any color in a continuous range, and color switching is not instantaneous. One key question is whether the additional degrees of freedom of the RD models predict nontrivial features of the dynamical system that cannot be captured by the sCA or Lenz-Ising models.

Here, we numerically investigate the dynamics of the RD models and show that, within the two large clusters of green and black scales, unsuspected subclusters in color distribution are forming as the pattern approaches steady state. The difference of color between scales belonging to different subclusters is very small but entirely and unambiguously defined by the general state (green or black) of the scales' neighbors. Analyzing the colors of individual scales of real lizards with hyperspectral imaging, we show that this subtle neighborhood-dependent color subclustering (not visible with the naked eye) is indeed present in these animals, confirming the nontrivial prediction of the numerical model. In addition, using an extensive set of histological serial sections, we show that the depth of melanophores within a scale correlates with the identity of the color subcluster to which the scale belongs, confirming that numerically predicted color subclustering is indeed associated to the state of the system at the cellular level. We also show that, under the constraint of periodic variation of the domain thickness, the observed subclustering is a general attribute that can be effectively captured by RD, regardless of the RD equation form, discretization, and spatial dimensionality. Finally, we show that RD parameter values determine the orientation of the correlation between green-scale blackness and the number of isochromatic neighbors, and that sets of parameter values generating correct direction of subclustering (i.e., as observed in real lizards) can be identified in the 12-dimensional RD parameter space, hence instructing the mathematical model.

II. NUMERICAL MODELING

A. Steady-state scale color distribution exhibits neighborhood-dependent subclustering

First, we modify the quasihexagonal pattern of a juvenile ocellated lizard such that it occupies a regular strictly hexagonal lattice and we arbitrarily assign the values (U, V, W) of green and black scales to (1.82, 6.29, 2.42) and (4.93, 1.55, 3.93), respectively. Using this pattern as initial condition [Fig. 1(b)], we apply the dRD model [24] to numerically investigate the dynamics of continuous color change (see Sec. VI). At the steady state of the patterning process [left-hand panel in Fig. 1(c)], each scale seems to take one of two colors (black with high values of U and W, and green with high value of V). This feature is a consequence of the fact that the Turing length scale L_T of the dRD model is close to the lattice spacing length scale (see Appendix A 1). However, finer examination of the RD component densities [Figs. 1(d) and 1(e) and right-hand panel in Fig. 1(c)] indicates a definite nonoverlapping subclustering. Remarkably, this arrangement is entirely defined by the nearest-neighbor configurations of scales: black scales with the same number of black neighbors belong to the same black subcluster. Similarly, green scales with the same number of green neighbors belong to the same green subcluster. This phenomenon is independent from initial condition as (i) steady-state subclustering is also observed (Supplemental Material, Fig. S1 [34]) when starting from all scales very close to the unstable homogeneous steady state $(U, V, W) = (3.51, 2.96, 3.45)$ and (ii) the positions of the final subclusters in (U, V, W) can be analytically approximated [white crosses in Fig. 1(e) herein and Supplemental Material, Fig. S1D [34]; see also Appendix A 2]. Note that clustering is visible at the next hierarchical level [i.e., subsubclustering, inset in Fig. 1(e)] and is due to second-neighbor configurations.

The time evolution also exhibits dynamic subclustering [Fig. 1(d)]: green scales (initially set to the same color, see above) with different numbers of green neighbors (seven possibilities: $n_G = 0$ to $n_G = 6$) separate as they move with different rates toward one of the green subclusters or shift color and move to one of the black subclusters. A similar separation of seven "lineages" is observed for black scales [Fig. 1(d), inset (i)]. Furthermore, because their neighbors can also change color, scales initially with the same early configuration (say, $n_G = 6$) can experience shifts in neighborhood state such that sites, transiently of similar colors, disperse in the form of a series of fuzzy sublineages [Fig. 1(d), inset (ii)] corresponding to the acquisition of distinct neighborhoods. Note that, when starting with all sites close to the unstable homogeneous steady state (i.e., an unclustered initial condition; see Supplemental Material Fig. S1 [34]), scales disperse much more homogeneously, i.e., they occupy a much larger range of colors, but finally also settle in one of the black or green subclusters.

B. Heterogeneity of edge lengths causes increased dispersion of subclusters

As renormalization of the diffusion term in the dRD model involves the hexagonal side length [Eqs. (11) and (12)], we propose that the observed nonoverlapping

subclustering of scale colors in hexagonal regular lattices [Figs. 1(d) and 1(e)] is due to the discrete distribution of

$$\mathcal{L}_k = \sum_{k'} \delta_{s_k s_{k'}} L_{kk'}, \tag{1}$$

where

$$s_k = \begin{cases} 1 & \text{if } k \text{ green } (V_k > 4.5) \\ 0 & \text{if } k \text{ black } (V_k \leq 4.5), \end{cases}$$

i.e., the sum of side lengths $L_{kk'}$ that polygon k shares with first-neighbor polygons k' of the same general color (green or black) as k (in the above formula, δ_{ij} denotes the Kronecker delta function). To test this hypothesis, we first generalize the dRD model to arbitrary edge lengths and lattices of arbitrary polygonal order distribution [see Eq. (10)]. Second, starting from the regular hexagonal tiling, we perturb the hexagon center coordinates with noise of varying amplitude. Running the dRD model to steady state on the Voronoi diagrams defined by the displaced

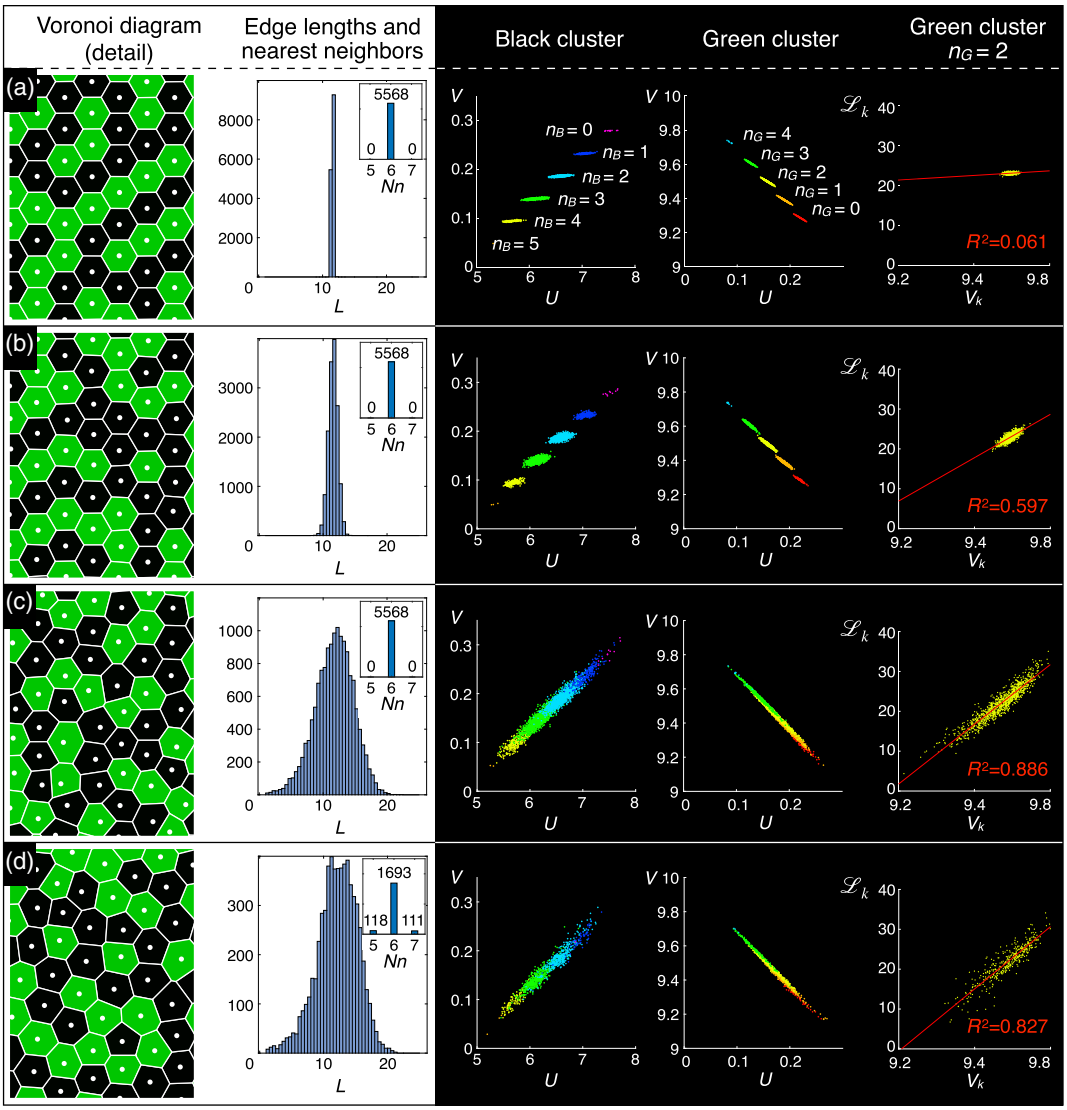


FIG. 2. Geometry perturbations increase dispersion of subclusters. Steady-state subclustering of the black and green clusters in four different geometries. (a) Weakly perturbed hexagonal lattice, (b) mildly perturbed hexagonal lattice, (c) strongly perturbed hexagonal lattice, and (d) Voronoi diagram of skin-scale positions on an actual ocellated lizard. From left to right, we show (i) a detail of the lattice with steady-state colors, (ii) the distribution of edge lengths L (inset: distribution of the number of edges Nn of the polygons), (iii) the black cluster in (U, V) projection, (iv) the green cluster in (U, V) projection, and (v) for the $n_G = 2$ green subcluster: the correlation between the steady-state value V_k and the total length $\mathcal{L}_k$ of edges in Eq. (1) that each polygon shares with neighbors of the same color. This correlation between (U, V, W) and $\mathcal{L}_k$ explains overlapping between subclusters in strongly irregular geometries (c),(d). Note that the 3D distribution graphs in (U, V, W) space of all scales are provided as Supplemental Material, Files S2–S5 [34] for (a)–(d).

hexagon centers shows that the correlation between position in (U, V, W) space and neighborhood configuration is maintained but the subclusters increasingly overlap as the noise is made larger [Figs. 2(a)–2(c)]. Third, as heterogeneity in polygonal order causes heterogeneity of $\mathcal{L}_k$, we simulate the dRD model on the quasihexagonal Voronoi diagram reconstructed from the surface scanning [35] of a real ocellated lizard [Fig. 2(d)]: here again, correlation between scale color and neighborhood configuration is maintained but subclusters overlap. Fourth, we identify a strong correlation between the color of a scale k (illustrated for the value V in the rightmost panels of Fig. 2) and its corresponding $\mathcal{L}_k$, indicating that increased dispersion of clusters is indeed due to heterogeneity in the sum of side lengths that scales share with their same-color neighbors. The dependence of subclustering on $\mathcal{L}_k$ is also analytically investigated in Appendix A 2. Note that stochastic noise in components' concentrations can amplify the overlap between subclusters (Supplemental Material, Fig. S2 [34]).

To exclude the possibility that the color subclustering phenomenon is caused by the spatial discretization of the dRD model or its 2D nature, we performed cRD simulations in a bona fide 3D hexagonal lattice of ≈500 bell-shaped scales (Supplemental Material, Figs. S3A and S3B [34]). After running the model to stable steady state (Supplemental Material, Figs. S3C and S3D [34]), we estimate the color of each scale by separately averaging the (u, v, w) values within its central region (i.e., covering 30% of its surface). Plotting the positions of scales in mean (u, v, w) space confirms the results outlined above with the 2D dRD model: scales form color subclusters (Supplemental Material, Fig. S3E [34]). Note that we observe this subclustering phenomenon even when we substantially transform the form of the reaction term, e.g., when performing cRD simulations with the Gray-Scott [36,37] or the Gierer-Meinhardt [3] models (Supplemental Material, Fig. S4 [34], left-hand and central columns) which incorporate only two RD components. Patterns in these two models are established through diffusion instability (i.e., the so-called "Turing instability") as in the three-component model used here for ocellated lizards. In addition, we observe the subclustering phenomenon even for the one-component Allen-Cahn equation [38] (Supplemental Material, Fig. S4, right-hand column [34]) in which nonlinearity is introduced in the form of two competing stable steady states: starting from the unstable steady state with noise, domains of different colors develop by attraction of the initial fluctuations toward one or the other stable steady state, with domain boundaries forming and stabilizing in the interscale regions. Hence, as far as scaled-skin color patterning is concerned (i.e., with its substantial interscale diffusion restriction), we can safely suggest that the observed subclustering is a generic feature (reflecting the interplay between diffusion and spatial near-discretization) that is efficiently captured by RD models, irrespective of their form, discretization, and spatial dimensionality. Importantly, our analyses additionally indicate that the orientation in RD components' space of this correlation (between scales greenness or blackness and the number of isochromatic neighbors) can differ depending on the model used, but also as a function of the values of parameters within a model (see Sec. IV and Appendix C).

We conclude that, first, on a regular hexagonal lattice, the RD steady-state color distribution of scales forms two principal clusters (black vs green), each of which is decomposed into seven subclusters corresponding to the seven possible neighborhood configurations of a hexagon. Note that not all possible subclusters are necessarily populated at all stages of the dynamics. For example, steady-state frequencies of black scales with 6 black neighbors, or of green scales with 5 or 6 green neighbors, are very rare [24]. Second, we show that for irregular hexagonal or nearly hexagonal lattices, the (U, V, W) steady-state values of scales still strongly correlate with their neighborhood configuration, but dispersion of the subclusters increases with the heterogeneity in the sum of side lengths that scales share with their isochromatic first neighbors. When heterogeneity is large enough, the subclusters overlap.

III. BIOLOGICAL EXPERIMENTS

A. Real lizards exhibit neighborhood-dependent subclustering of scale color

To test in real lizards the above theoretical conjecture of neighborhood-dependent color subclustering, we performed hyperspectral imaging on the dorsal skin of five ocellated lizards: two mature males (3 and 5 years old), one mature female (5 years old), one adolescent male (2.5 years old), and one juvenile (5 months). The three first individuals were old enough for their pattern to likely be close to steady state [24]. However, given that the color switching of any given scale is much faster than the overall patterning process, it is likely that individual green and black scales are at a transient steady-state color (until the next color shift) at any time point, even if the pattern itself is not at steady state. Hence, all used individuals might be adequate to test our conjecture as long as brown scales (i.e., in the process of shifting from green to black or vice versa) are excluded. The five individuals were sacrificed, their dorsal skin was removed, submerged in phosphate-buffered saline, and positioned under a microscope at 5× magnification with reflected illumination. Images were captured with a hyperspectral camera in a spectral range $\lambda = 462, 466, 470, \ldots, 702$ nm, i.e., with a 4 nm spectral sampling. Hyperspectral imaging provides much more detailed information on reflectance spectra than simple RGB imaging. For each lizard, green scales with $n_G = 1$, 2, 3, 4 green nearest neighbors were randomly selected [Fig. 3(a) herein and Supplemental Material, Table S1 [34]]. As green scales with $n_G = 0, 5, 6, \ldots$ are scarce in the observed patterns, they were not considered in the

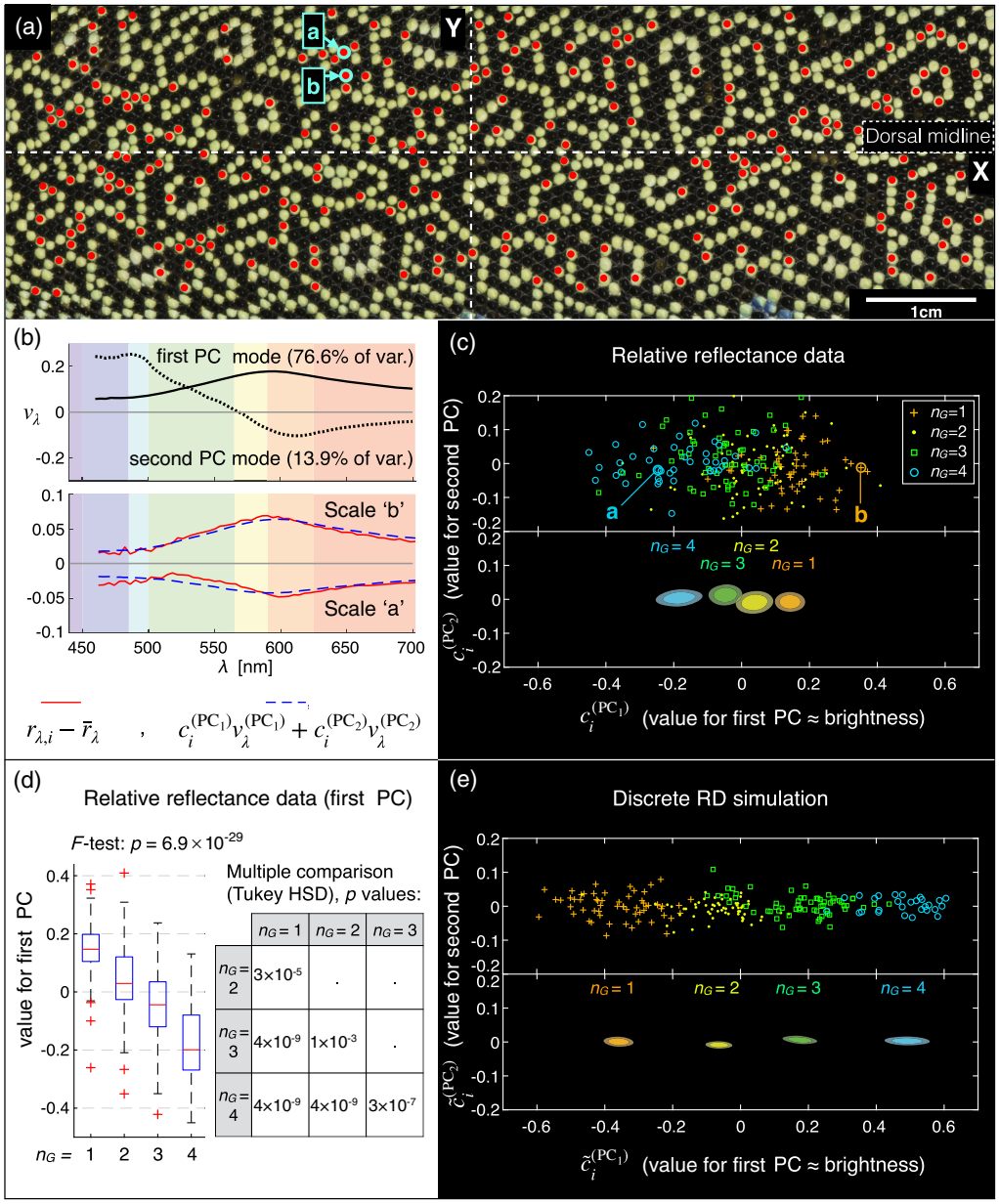


FIG. 3. Neighborhood-dependent scale color subclustering in real lizards. (a) Dorsal skin of an ocellated lizard (individual TL66) with a sample of 224 skin scales marked in red. Scales "a" and "b" are examples of neighborhood configurations $n_G = 4$ ("a") and $n_G = 1$ ("b"). (b) Top: spectral modes associated to the first (solid line) and second (dashed line) principal components (PC) accounting for 90.6% of the dataset total variance. Bottom: deviation from the mean $(r_{\lambda,i} - \bar{r}_\lambda)$ of relative reflectance spectra (red solid line) and its projection on the first two PCs (blue dashed line) for scales "a" and "b". (c) Top: coordinates of first two PCs for relative reflectance data, colored according to nearest-neighbor configurations $n_G = 1, 2, 3, 4$; scales "a" and "b" are indicated. Bottom: Bayesian credibility ellipses for clusters' averages of the same data ($p = 0.9$ for inner ellipses, $p = 0.99$ for outer ellipses). The first PC strongly correlates with neighborhood configuration. (d) Left: box plot and analysis of variance (F-test) for first PC data; clusters' averages are significantly different. Right: p values for Tukey-Kramer honestly significant difference (Tukey HSD) tests of pairwise comparisons between clusters' averages. (e) Top: coordinates of first two PCs [dimensional reduction of (U, V, W) space] for simulated data [dRD on real lizard Voronoi diagram of Fig. 2(d)]; data points with different neighborhoods are sampled with the same frequencies as in real data (c). Bottom: Bayesian credibility ellipses represented as in (c). The origin of the inverse correlation with nearest-neighbor configurations of simulated (e) vs observed (c) data is analyzed in Sec. IV.

analysis. Note that black scales' reflectance was too low to allow for subclustering analysis.

The relative reflectance spectra of all selected green scales [i.e., the data $R_i(\lambda)$ for $i = 1, \ldots, N_{\text{scales}}$] were then measured by averaging in each scale the spectra of about 40 pixels covering the central 30% of its surface. We then observed a correlation between green scale reflectance and their position on the animal (corresponding

to wavelength-specific dorso-lateral and cephalo-caudal reflectance gradients). To correct for these nuisance parameters, we fit a quadratic slowly varying function $R^{\mathrm{pos}}(\lambda, x_i, |y_i|)$ to the spatioreflectance data $\{(x_i, y_i), R_i(\lambda)\}_{i=1,\ldots,N_{\mathrm{scales}}}$. Examples of such functions are illustrated in Supplemental Material, Fig. S5 [34]. To test whether the remaining variation $r_{\lambda,i} = R_i(\lambda) - R^{\mathrm{pos}}(\lambda, x_i, |y_i|)$ is correlated to scale neighborhood state, we perform a dimensionality reduction using principal component analysis (PCA; see Sec. VI): we construct the covariance matrix of the data $r_{\lambda,i}$ and identify the two eigenvectors $v_\lambda^{(\mathrm{PC}_{1,2})}$ (principal directions) associated to the largest eigenvalues. We then project the data on this subspace: $r_{\lambda,i} \approx \bar{r}_\lambda + c_i^{(\mathrm{PC}_1)} v_\lambda^{(\mathrm{PC}_1)} + c_i^{(\mathrm{PC}_2)} v_\lambda^{(\mathrm{PC}_2)}$. These two principal components (PC_1 and PC_2) account for 90.6%–96.6% (depending on the lizard individual) of the variance in the spatially corrected hyperspectral reflectance data (Supplemental Material, Table S1 [34]), and therefore represent it accurately [Fig. 3(b)]. Note that the first principal component PC_1 can be interpreted as a brightness correction, so may represent melanophore contribution (U in the model), and the second PC_2 as a hue correction that can be interpreted as xanthophore contribution (V in the model).

Each scale is represented by a point $(c_i^{(\mathrm{PC}_1)}, c_i^{(\mathrm{PC}_2)})$ in the PC_1-PC_2 plane [Fig. 3(c)] and is color labeled according to its number of green neighbors (n_G); Bayesian credibility ellipses (see Sec. VI) are indicated for each corresponding group. Remarkably, PC_1 strongly correlates with n_G: the clusters' averages are well separated along the PC_1 axis and, for most of the pairwise comparisons between groups, the outer ellipses do not overlap [Fig. 3(c)], indicating that the two groups have a posterior probability $< 10^{-4}$ to be sampled from bivariate normal distributions with the same mean (i.e., scales with the corresponding two different neighborhood configurations have significantly different shades of green). These results are corroborated by a standard analysis of variance (F-test) and pairwise Tukey-Kramer tests [Fig. 3(d)] for PC_1. Finally, we applied a standard Fisher linear discriminant analysis (FLDA) on the unreduced centred data $r_{\lambda,i} - \bar{r}_\lambda$ to find the spectral mode which best separates the groups (see Sec. VI). As often observed with FLDA, the main discriminant mode explains a much lower proportion of the total variance than PC_1, but it separates the groups with higher statistical significance (Supplemental Material, Fig. S6 [34]). Note that performing the same analyses (Bayesian credibility ellipses, analysis of variance, pairwise Tukey-Kramer tests, and FLDA) with raw data, i.e., without correction for spatial dependence of the reflectance data, generates similar conclusions albeit with slightly lower statistical significance (Supplemental Material, Fig. S7 [34]).

It is remarkable that the subtle neighborhood-dependent color subclustering predicted by numerical simulations is detectable in real lizards despite (i) the noise associated to hyperspectral measurements and (ii) the multitude of underlying biological variables. Note that identical hyperspectral data acquisition procedures and analyses with four additional lizard individuals indicate (Supplemental Material, Fig. S8 [34]) that three of these four animals also exhibit highly significant neighborhood-dependent subclustering of green-scale hyperspectral reflectance. Finally, performing the same PCA analyses [Fig. 3(e)]—as well as F-test, Tukey-Kramer tests, and FLDA (Supplemental Material, Fig. S9 [34])—on the (U, V, W) data numerically simulated on a realistic quasihexagonal 2D lattice [Fig. 2(d)] generates subclustering along the two first PCs (indicated as $\tilde{c}_i^{(\mathrm{PC}_1)}$ and $\tilde{c}_i^{(\mathrm{PC}_2)}$) similarly to the experimental reflectance data [Fig. 3(c)], albeit with (i) less overlap between subclusters and (ii) an inverse correlation between green-scale brightness and nearest-neighbor configuration. The origin of this inversion is identified and analyzed in Sec. IV, allowing us to instruct the mathematical model.

B. Melanophore distribution within scales correlates with color subclustering

As (i) the color of skin scales is determined by their chromatophore composition [12–16] and (ii) the values of U and V are intended to model the densities of chromatophores, the RD system used above predicts the existence, in real ocellated lizards, of a neighborhood dependence not only of mesoscopic measurement of skin scales' hyperspectral reflectance (as identified above), but also of microscopic parameters associated with chromatophore organization within skin scales. Hence, we performed histological serial sectioning of green scales belonging to different hyperspectral subclusters and tested if distributions of chromatophores depend on the neighborhood of the corresponding scales. More specifically, the dorsal skin of one animal used for hyperspectral analyses [Figs. 3(a)–3(d)] was fixed in formalin and 41 green scales with different neighborhoods (14, 8, 6, and 13 scales with $n_G = 1, 2, 3$, and 4, respectively) were sampled, dehydrated in ethanol, embedded in paraffin blocks, sectioned at 7 μm, stained with hematoxylin and eosin (HE), and imaged at a spatial resolution of 0.23 μm/pixel to generate a high-quality set of 3845 images (mean = 94 sections/scale). A single section across three adjacent scales is illustrated in Fig. 4(a). Each image of each scale section was color segmented (see Sec. VI) to identify the epidermis as well as pixels belonging to melanophores or iridophores [Fig. 4(b), top left]. A 3D model [i.e., in full XYZ space, Fig. 4(b), top right] of each of the 41 scales was reconstructed using rigid transformations (guided by melanophore and iridophore distributions) between consecutive XZ sections. After transforming each labeled XZ pixel into a voxel of $(0.23 \times 0.23 \times 7)$ μm^3, we fitted algebraically an ellipse to the XY projection of the scale boundary, and we restricted the volumetric data to the voxels both situated below the epidermis and whose XY projection falls inside the central 25% of the scale [Fig. 4(b), top and

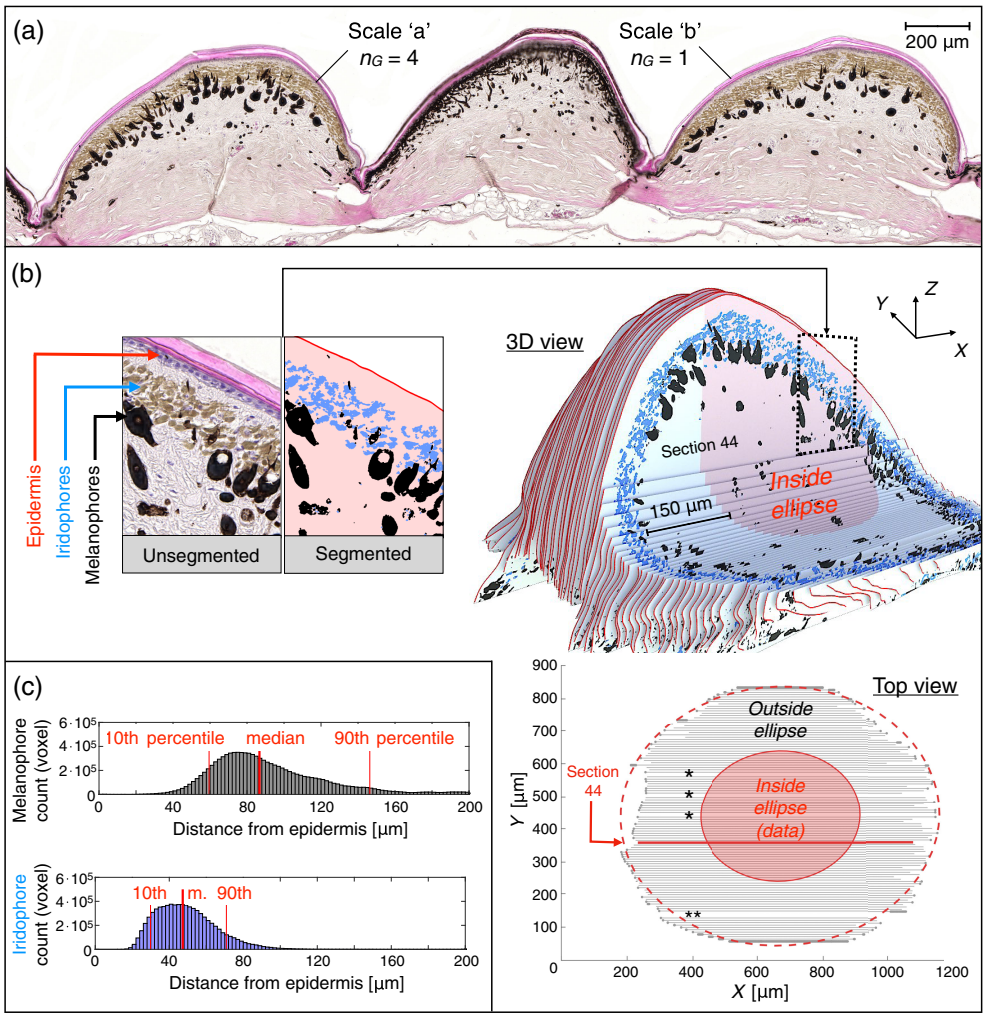


FIG. 4. Histological analysis of chromatophore spatial distribution in lizard skin scales. (a) Example of histological section (HE staining) through scales "a" and "b". (b) Segmentation (black, melanophores; blue, iridophores; red, epidermis) and alignment of sections for reconstruction of skin-scale chromatophore distribution. Left: a detail of raw image of section and its color segmentation. Top right: alignment of segmented sections for 3D reconstruction of the skin scale; a large proportion of each section in front of no. 44 is made transparent. The region of interest ("inside ellipse") used for extraction of chromatophore distribution is indicated in light red. Bottom right: top view of the same alignment of sections, highlighting the construction of the light red ellipse used for data extraction. Stars indicate missing sections. (c) Spatial distribution of chromatophores (distance from epidermis of each labeled voxel) extracted from light red region. The 10th, 50th, and 90th percentiles are indicated.

bottom right-hand panels]. We then computed the volume fractions, and distributions of distance to the epidermis, of melanophores and iridophores in each scale [Fig. 4(c)].

We observe that measurements pertaining to melanophores are strongly correlated with scale neighborhood state: Bayesian credibility ellipses show that melanophore data [Fig. 5(a)] are very unlikely sampled from bivariate (median distances to epidermis and volume fraction) normal distributions with the same mean for different neighborhood configurations (posterior probability $\ll 10^{-4}$ for green scales with $n_G = 1$ vs $n_G = 4$, and posterior probability $\ll 10^{-3}$ for $n_G = 1$ vs $n_G = 3$ or $n_G = 2$ vs $n_G = 4$). Note that these results are qualitatively perceptible by eye when comparing the left and right green scales ($n_G = 1$ vs $n_G = 4$) in Fig. 4(a). Similarly, (i) an F-test performed on the grouped data strongly rejects [$p = 1.8 \times 10^{-6}$ for median distance, Fig. 5(b), and $p = 6.6 \times 10^{-8}$ for volume fraction, Supplemental Material, Fig. S10 [34]] the hypothesis that the groups are sampled from normal distributions with equal means, and (ii) the groups identified as significantly different by pairwise Tukey-Kramer tests [Fig. 5(b) herein and Supplemental Material, Fig. S10 [34]] are the same as those identified by the Bayesian analyses. Although the same statistics (volume fraction and distance to epidermis) were mostly nonsignificant for iridophores, the most significant neighborhood dependence was observed for the ratio of the

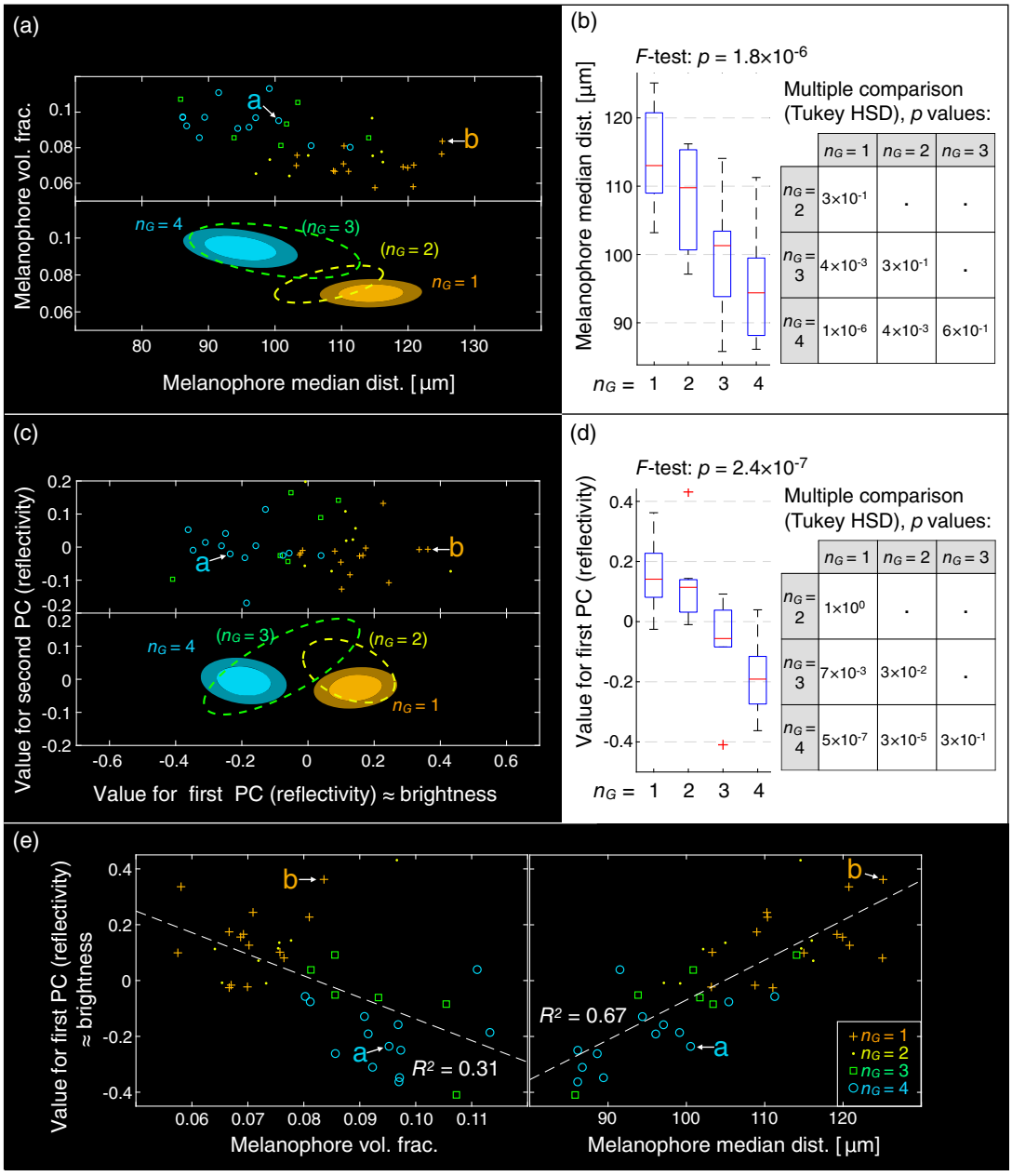


FIG. 5. Melanophore distribution and comparison with reflectance results. (a) Top: median distance to epidermis and volume fraction of voxels labeled as "melanophore" for each of the 41 skin scales (individual TL66) selected for histology. Bottom: Bayesian credibility ellipses for cluster averages of the same data, grouped according to nearest-neighbor configuration ($p = 0.9$ for inner ellipses and dashed ellipses, $p = 0.99$ for outer ellipses). (b) Box plot, analysis of variance (F-test, cluster averages are significantly different) and p values for Tukey-Kramer pairwise comparison tests between cluster averages for melanophore distance data. See Supplemental Material, Fig. S10 [34], for melanophore volume fraction analysis. (c) PCA of relative reflectance data [as in Fig. 3(c)] for this subset of 41 skin scales and (d) corresponding box plot, analysis of variance (F-test) and Tukey-Kramer pairwise comparison for first PC of relative reflectance data. The significance level of clustering is similar to that of melanophore distance in (b) and melanophore volume fraction in Supplemental Material Fig. S10 [34]. (e) Correlation between reflectance data (first PC) and melanophore volume fraction (left) or median distance to epidermis (right). Scales "a" and "b" are indicated in (a), (c), and (e).

characteristic distance of iridophores over that of melanophores (especially tenth percentile distances; see Supplemental Material, Fig. S11 [34]). This increase in significance may indicate that (i) taking ratios of distances removes part of the noise due to size variation of skin scales and (ii) the subtle differences of color among green scales with different neighborhoods is mostly attributable to the chromatophores closest to the epidermis.

Remarkably, the dependence of melanophore statistics on scale neighborhood is of similar statistical significance

in comparison to the neighborhood dependence on perceived color for the same dataset: PCA of the hyperspectral data restricted to the 41 sectioned green scales indicates that (i) PC_1 of the spatially corrected reflectivity spectrum correlates with scale neighborhood [Fig. 5(c)], (ii) an F-test rejects the null hypothesis that the data from the different groups are sampled from distributions with the same mean [Fig. 5(d)], and (iii) Bayesian credibility ellipses [Fig. 5(c)] and pairwise Tukey-Kramer tests [Fig. 5(d)] statistically distinguish the same groups as with the histology data. Unsurprisingly, these statistics are less significant than when considering the full dataset of 224 scales (Fig. 3), but a key observation is that the same statistical tests on hyperspectral analyses and melanophore measurements for the same restricted number of scales show similar significance. Finally, the first principal component of the reflectance data (PC_1) strongly correlates with both melanophore volume fraction and melanophore median distance to the epidermis [Fig. 5(e)], confirming the link between mesoscopic and microscopic measurements.

IV. OBSERVED CORRELATION ORIENTATION INSTRUCTS THE MATHEMATICAL MODEL

The hyperspectral and histological data collected from actual lizards clearly show that, as their number of green nearest neighbors increases, green skin scales tend to have increased blackness [i.e., decreased brightness; see Figs. 3(c) and 5], because of the corresponding increase in melanophore volume density and proximity to the epidermis. However, the RD system with parameter values classically used to model the skin color patterning in ocellated lizards [24,25,33] predicts the *opposite* correlation, i.e., a *decrease* of blackness of green scales with an increased number of green nearest neighbors [Figs. 1(d), 1(e), and 3(e)]. Note that these parameter values were previously fixed by optimization procedures which only took into account the spatial distribution of green and black scales in the final pattern (quantified using nearest-neighbor statistics), and not the finer dependence of scales' color on their neighborhood (which was only measured here for the first time). We show below that this correlation can be in almost any direction, and strongly depends on the numerical values of the "reaction parameters" of the system. Hence, we propose here that the correlation observed in real lizards can instruct the mathematical model of Ref. [17] by helping identify chromatophore interactions (and corresponding effective parameter values) of the RD system that better fit with the biological observations. More specifically, we investigate the two following questions. (Q1) Can we find parameters giving both natural nearest-neighbor statistics of the overall pattern *and* correct direction (i.e., as observed in real lizards) of correlation between green-scale blackness and their number of green neighbors? (Q2) Are there chromatophore interactions in the model that most influence the direction of this correlation? To answer these questions, we perform a large scan inside the allowed reaction parameter space, given by the signs of interaction parameters [Fig. 1(a)] fixed by laser ablation experiments in zebrafish [17]. We pay special attention to parameter c_5 (i.e., long-range influence of melanophores on xanthophores) which may, in principle, be positive or negative, but is usually set to 0 because it remained undetermined from these experiments [17].

To evaluate the capacity of the dRD model to generate patterns, we use the semianalytic method given in Appendix A 2: the existence of a solution for the main cluster Eq. (A14) indicates that stationary patterns are sustained. This approach allows rejecting a very large set of non-pattern-forming parameter values without the need of performing time-consuming numerical simulations. We then explicitly simulate, for the nonrejected parameter values, the dRD system on a 32×16 hexagonal lattice with initial conditions given by small perturbations of the homogeneous steady state identified with Eq. (A1). We then select the parameter values which give patterns (i) having reached stationarity before a large arbitrary limit of 15 000 time units, and (ii) exhibiting natural nearest-neighbor statistics, i.e., statistics very similar to those of actual adult lizards (Supplemental Material, Fig. S12 [34]). Concretely, we scanned through 345 600 000 parameter sets randomly drawn from a uniform distribution in the box:

$$\begin{aligned} c_1, c_2, c_4, c_8 &\in [-0.25, 0], \\ c_7, c_u, c_v, c_w &\in [0, 0.25], \\ c_3, c_6, c_9 &\in [0, 1], \\ c_5 &\in [-0.25, 0.25]. \end{aligned} \tag{2}$$

Besides c_5, which is usually set to 0, these values are typical orders of magnitudes used in previous studies [24,25,33]. The density of this sampling is equivalent to a grid scan with increment ≈ 0.073 in all varied parameters. The diffusion parameters of the dRD model are fixed [39] to values similar to those found in Ref. [33]: $d_u = d_v = 0.000\,125$, $d_w = 0.009$. Among the 345 600 000 randomly drawn parameter sets, 1412 give good nearest-neighbor statistics, among which 160 give the correct and 1194 give the incorrect, blackness correlation direction, respectively [Fig. 6(a)]. An example of a set of parameter values giving natural patterns and correct correlation is shown in Fig. 6(b).

First, these results indicate that correct blackness correlation can occur with a large variety of (natural and non-natural) nearest-neighbor statistics (Supplemental Material, Fig. S13 [34]). Second, correct blackness correlation direction is not the most common feature in the sampled box, both for generic patterns (3021 out of 25 890, i.e., 12%; Supplemental Material, Fig. S13A [34]) and for patterns with natural nearest-neighbor statistics (160 out of 1412, i.e., 11%; Fig. 6(a) herein and Supplemental Material, Fig. S13B [34]). Hence, these results answer question Q1 above: we can indeed find parameters giving

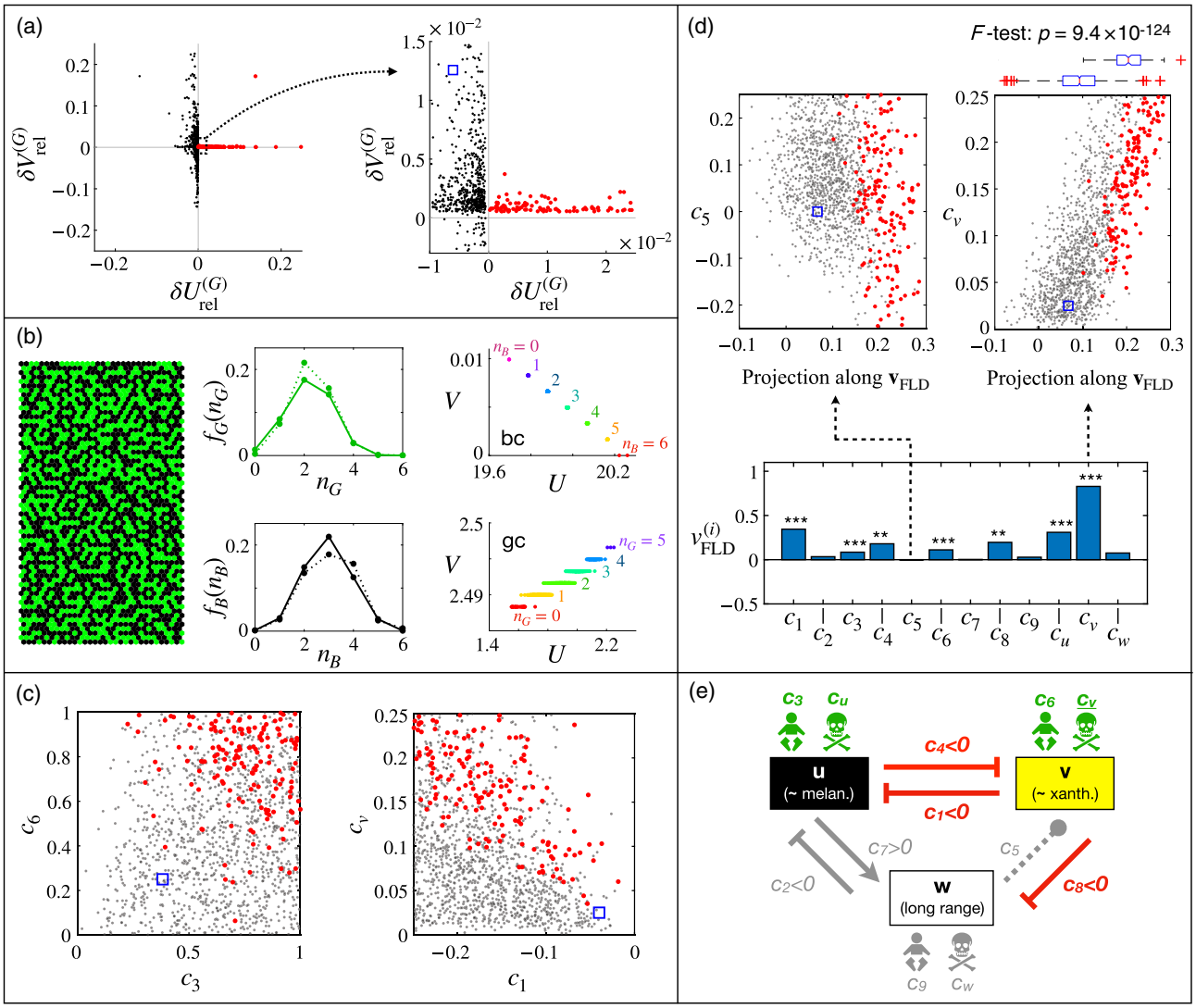


FIG. 6. Scanning of the dRD system for correct correlation between green-scale blackness and neighborhood configuration. (a) Left: green subcluster correlation direction $(\delta U^{(G)}_{\mathrm{rel}}, \delta V^{(G)}_{\mathrm{rel}})$ in U and V directions for sets of parameter values associated to natural nearest-neighbor statistics; right: enlargement close to origin. Red and black data points are the 160 and 1194 sets giving correct and incorrect correlation directions, respectively. Note that 58 sets have undetermined correlation. No set simultaneously gives both $\delta U^{(G)}_{\mathrm{rel}} > 0$ and $\delta V^{(G)}_{\mathrm{rel}} < 0$. (b) An example of good parameter set ($c_1 = -0.228\,10$, $c_2 = -0.026\,10$, $c_3 = 0.638\,61$, $c_4 = -0.173\,65$, $c_5 = 0.219\,50$, $c_6 = 0.834\,67$, $c_7 = 0.043\,27$, $c_8 = -0.086\,29$, $c_9 = 0.129\,75$, $c_u = 0.024\,67$, $c_v = 0.200\,14$, $c_w = 0.089\,55$). Left: steady-state pattern. Middle: corresponding nearest-neighbor statistics (solid lines) compared to those observed in an adult lizard (dotted lines) for both green (top) and black (bottom) scales. Right: U and V values of black (top) and green (bottom) subclusters, colored according to the number of isochromatic nearest neighbors. The green cluster (gc) has correct blackness (U direction) correlation. (C) Parameter sets with natural nearest-neighbor statistics, colored according to correct (red) or incorrect (black) blackness correlation direction. Production rates c_3 and c_6 (left), decay rate c_v and interaction c_1 (right) influence blackness correlation. (d) Lower panel: components of the Fisher linear discriminant direction $\mathbf{v}_{\mathrm{FLD}}$ best separating the sets with correct and incorrect blackness correlation directions; significant (bootstrapping, 10 000 random resamplings) nonzero coordinates are annotated with stars (*, $p \in [0.05, 0.01]$; **, $p \in [0.01, 0.001]$; ***, $p < 0.001$). F-test value for the discrimination of correct vs incorrect correlations in the FLD direction is indicated. Upper panels: projections along $\boldsymbol{v}_{\mathrm{FLD}}$ for parameters c_v and c_5 that, respectively, most and least influence blackness correlation [correct (incorrect) directions are labeled in red (black)]. (e) $\boldsymbol{v}_{\mathrm{FLD}}$ in (d) identifies the interaction (positive and negative arrows), production (baby icon), and decay (crossbones) terms whose absolute value should be increased (green) or decreased (red) to obtain correct correlation direction; i.e., all colored parameters should see their (nonabsolute) value increased, as visible in the bottom panel of (d). The blue square in (a), (c), and (d) indicates the set used in Figs. 1 and 2 giving incorrect blackness correlation of the green subclusters.

both natural nearest-neighbor statistics *and* correct direction of correlation between blackness of green scales and their number of green neighbors. Note that the shape of the interaction terms of the reaction function close to the green or black steady states strongly influences subclustering correlation (see Appendix A 2 for an analytic investigation of this effect).

Third, to determine which parameters [e.g., c_1, c_3, c_6, c_v; Fig. 6(c)] influence the most the correlation direction, we compute the Fisher linear discriminant direction ($\boldsymbol{v}_{\mathrm{FLD}}$) which best separates the two groups of 160 parameter sets with correct correlation direction vs 1194 sets with incorrect direction (the 58 sets with undetermined direction are ignored). We find that significantly nonzero $\boldsymbol{v}_{\mathrm{FLD}}$ components are given by $c_1, c_3, c_4, c_6, c_8, c_u, c_v$ [Fig. 6(d)], hence, answering question Q2. These correspond, in the interaction network of Fig. 6(e), to the decrease of the effective inhibitions c_1, c_4, and c_8 (i.e., an increase of their values), the increase of the effective productions c_3 and c_6, and the increase of the effective decays c_u and c_v, the latter being the most dominant parameter [Fig. 6(d)]. In other words, if one uses a set of parameter values that yield an incorrect correlation between green-scale brightness and number of isochromatic neighbors, one must change the values of parameters $c_1, c_3, c_4, c_6, c_8, c_u, c_v$ by following the direction defined by $\boldsymbol{v}_{\mathrm{FLD}}$—in this case, increasing c_v would be the most effective single-parameter change. Note that the increase of xanthophore decay c_v remains the principal contribution to $\boldsymbol{v}_{\mathrm{FLD}}$ when we use more stringent definitions of "natural nearest-neighbor statistics" (Supplemental Material, Fig. S14 [34]). In addition, we show in Appendix C 2 that the partial overlap along $\boldsymbol{v}_{\mathrm{FLD}}$ between sets of parameter values with correct vs incorrect correlation directions [e.g., Figs. 6(c) and 6(d)] is due to the complexity of the boundary hypersurfaces in the 12-dimensional RD parameter space. Indeed, we confirmed that, locally, the hypersurfaces can be approximated by hyperplanes that sharply separate sets with correct vs incorrect correlations (Supplemental Material, Fig. S15 [34]).

V. DISCUSSION AND CONCLUSIONS

The combination of numerical simulations, experimental hyperspectral analyses, and investigations of chromatophore microscopic spatial distributions presented here demonstrate that a simple RD model on a lattice of sites does not only correctly and quantitatively describe both the dynamics of scale-by-scale color change and the time evolution of the ocellated lizard pattern [24,25,33], but it also produces accurate predictions of some real-life features at a much finer level of analysis, i.e., the presence of an unsuspected subtle subclustering of scale colors that correlates with the number of isochromatic nearest neighbors. The high predictability of the zebrafish three-component RD mathematical model [17] in describing the fine subclustering dynamics observed in ocellated lizards is surprising for at least three reasons. First, the ocellated lizard and zebrafish exhibit very different steady-state patterns. Second, squamate reptiles and teleost fishes are very distant evolutionary relatives as their common ancestor lived about 430 million years ago. Third, zebrafish and lizard chromatophores exhibit prominently different behaviors. For example, the color patterning of the zebrafish skin into stripes and interstripes involves the spatial segregation of melanophores, xanthophores, and two types of iridophores [40], whereas the color flipping of ocellated lizard's scales between green and black might not involve cell migration but a transition between two states of melanophores: condensed [i.e., with melanosomes gathered in the cell body in green scales; Fig. 4(a), left- and right-hand scales] vs dispersed [i.e., with melanosomes distributed in cellular protrusions extending to the epidermal-dermal interface in black scales; Fig. 4(a), central scale]. Histological sections also suggest that iridophores might form a thicker layer in green scales than in black scales, hinting at a possible role of cell proliferation and cell death. Yet, the zebrafish RD model, superposed to the geometry of the lizard's scaled skin [24,25,33] predicts scale-by-scale green-vs-black clustering as well as the finer subclustering uncovered here.

However, when used with classical parameter values, the RD model predicts the *opposite* correlation (in comparison to that observed in real lizards) between green-scale blackness and neighborhood configuration. Our scan of the 12-dimensional RD parameter space indicates that one can find multiple sets of parameter values that yield both natural nearest-neighbor statistics of the overall pattern *and* correct direction of scale-to-neighborhood correlation. In addition, we identify both the parameters that most influence the direction of this correlation and how their values must be adjusted to ensure correct correlation, hence, instructing the mathematical model.

It can be argued that the RD model used here is necessarily approximate, for zebrafish, ocellated lizard, or any other species, as it ignores the likely important role of iridophores [22,41–43] as well as a multitude of cellular and molecular actors, such as those (observed in zebrafish [21]) associated with the recognition, transport, and delivery of xanthoblast airineme vesicles to melanophores by macrophagelike relays. Yet, this implementation of the very simple and elegant RD mathematical framework, first proposed by Turing [1], properly captures multiple aspects of the dynamics and statistical features of the mesoscopic skin color patterning process in various species, despite their substantial differences at the cellular and/or molecular scales. In other words, our results show that subtle mesoscopic properties of biological dynamical systems, as well as some of the underlying microscopic features, are captured by simple numerically optimized RD models, and hence, can be efficiently predicted by numerical investigations, without integrating in the mathematical model the unmanageable profusion of variables at lower scales [44,45].

VI. METHODS

A. Animals and ethics statement

Ocellated lizards were bred in the laboratory at Department of Genetics and Evolution, University of Geneva, Switzerland. Maintenance of and experiments on animals were approved by the Geneva Veterinary Cantonal authorities (authorizations GE/82/14, GE/169/17, and GE24/33145) and performed according to the Swiss law. These guidelines meet international standards.

B. Generalized dRD model

A coarse-grained reaction-diffusion model, spatially discretized at the level of skin scales, was proposed in Ref. [24] for modeling dorsal skin scales as a perfect-hexagonal lattice. Also, in the same reference, a two-dimensional continuous reaction-diffusion model (2D cRD) was studied in which skin scales induced effective diffusion reduction in interscale regions. The dRD model was shown to be a good approximation of the 2D cRD [24] (see also Ref. [33] for dRD on general Voronoi diagrams), which in turn was shown to be a good approximation of a full-fledged reaction-diffusion model (3D cRD) on a three-dimensional domain with "bumps" representing skin scales by modulating domain thickness [25]. To streamline the logic, we show here how to directly obtain the dRD from the 3D cRD, and relate some key geometric quantities to the effective dRD diffusion coefficients. The procedure is essentially a finite-volume method that spatially discretizes the 3D cRD at the level of skin scales. Let us use the notation $u_n(\mathbf{x}, t)$ as the nth concentration involved in the 3D cRD, which is given by the partial differential equations:

$$\frac{\partial}{\partial t} u_n(\mathbf{x}, t) = F_n(u_1, u_2, \ldots) + D_n \nabla^2 u_n(\mathbf{x}, t). \tag{3}$$

No-flux spatial boundary conditions are assumed. The ∇^2 operator is the Laplacian operator in three dimensions. The term F_n is the "reaction" function, a local function of the concentrations, and D_n is the diffusion coefficient.

In cases where in the 3D cRD (i) the typical distance between neighboring skin scales is similar to, or smaller than, the Turing length scale and (ii) the reduction of thickness between skin scales is non-negligible, it is observed in numerical simulations that each skin-scale "bump" has typically, and most of the time, an approximately constant value of the concentrations u_n; i.e., large spatial variations of u_n are mostly restricted to the interscale regions. We therefore approximate the system using a finite-volume method, where each skin scale is a single finite-volume region $\mathcal{R}_k$ (Supplemental Material, Fig. S3A [34]). Integrating Eq. (3) over a region $\mathcal{R}_k$ and using the divergence theorem, we find

$$\int_{\mathcal{R}_k} d^3x \frac{\partial}{\partial t} u_n = \int_{\mathcal{R}_k} d^3x F_n(u_1, u_2, \ldots) + D_n \sum_{k'} \int_{\mathcal{S}_{kk'}} d^2x (\nabla u_n \cdot \mathbf{n}_{kk'}), \tag{4}$$

where $\mathcal{S}_{kk'}$ is the common surface between regions $\mathcal{R}_k$ and $\mathcal{R}_{k'}$ (see Supplemental Material, Fig. S3A [34]) which is empty if k and k' are not nearest neighbors, whereas $\mathbf{n}_{kk'}$ is the unit normal of $\mathcal{S}_{kk'}$. We define the volume and average concentrations:

$$V_k = \int_{\mathcal{R}_k} d^3x, \qquad U_n^{(k)} = \frac{1}{V_k} \int_{\mathcal{R}_k} u_n d^3x. \tag{5}$$

Since we assume that the concentrations do not vary a lot inside most of the skin scales, we use the following approximations:

$$\int_{\mathcal{R}_k} d^3x F_n(u_1, u_2, \ldots) \approx V_k F_n(U_1^{(k)}, U_2^{(k)}, \ldots),$$
$$\int_{\mathcal{S}_{kk'}} d^2x (\nabla u_n \cdot \mathbf{n}_{kk'}) \approx \frac{S_{kk'}}{\epsilon} (U_n^{(k')} - U_n^{(k)}), \tag{6}$$

where $S_{kk'}$ is the area of the common surface $\mathcal{S}_{kk'}$ (or 0 if k and k' are not nearest neighbors), and ϵ is the thickness of the thin interscale region where most of the spatial variation of concentrations occurs. For the second line of Eq. (6), we used a finite difference approximation across the band of length ϵ separating the two polygons: $\mathbf{n}_{kk'} \cdot \nabla u_n \approx (U_n^{(k')} - U_n^{(k)})/\epsilon$. Using Eqs. (5) and (6), the 3D cRD in Eq. (3) is approximated by the following dRD:

$$\frac{d}{dt} U_n^{(k)} = F_n(U_1^{(k)}, U_2^{(k)}, \ldots) + D_n \sum_{k'} \frac{S_{kk'}}{V_k \epsilon} (U_n^{(k')} - U_n^{(k)}). \tag{7}$$

The effective diffusion coefficients of the dRD at each link connecting two nearest neighbors are obtained by rescaling the actual diffusion coefficients by $S_{kk'}/(V_k \epsilon)$. To rewrite this in a way more similar to the formulas in Refs. [24,33], we assume that the domain is extended in the X and Y directions while the thickness modulation happens along the Z direction, and is given by a thickness function $z(x, y)$. The projections of $\mathcal{R}_k$ and $\mathcal{S}_{kk'}$ on the XY plane are denoted by $\tilde{\mathcal{R}}_k$ and $\tilde{\mathcal{S}}_{kk'}$, respectively. We define the skin-scale average thickness $z_k^{(s)}$ and the interscale average thickness $z_k^{(is)}$ as

$$z_k^{(s)} = \frac{1}{A_k}\int_{\tilde{\mathcal{R}}_k} z(x,y)d^2x = \frac{V_k}{A_k},$$
$$z_{kk'}^{(is)} = \frac{1}{L_{kk'}}\int_{\tilde{\mathcal{S}}_{kk'}} z(x,y)dr = \frac{S_{kk'}}{L_{kk'}}. \quad (8)$$

The geometric quantities A_k and $L_{kk'}$ are the two-dimensional skin-scale area and the edge length of the line separating two skin-scale projected domains:

$$A_k = \int_{\tilde{\mathcal{R}}_k} d^2x, \qquad L_{kk'} = \int_{\tilde{\mathcal{S}}_{kk'}} dr. \quad (9)$$

Let us assume that the average thicknesses are the same for all skin scales: $z_k^{(s)} = z^{(s)}$ and $z_{kk'}^{(is)} = z^{(is)}$. In terms of these two-dimensional geometric quantities, the dRD in Eq. (7) becomes

$$\frac{d}{dt}U_n^{(k)} = F_n(U_1^{(k)}, U_2^{(k)}, \ldots) + \frac{D_n P}{A_k \epsilon}\sum_{k'} L_{kk'}(U_n^{(k')} - U_n^{(k)}), \quad (10)$$

where $P = z^{(is)}/z^{(s)}$. The form in Eq. (10) is used in Ref. [33], where A_k and $L_{kk'}$ are interpreted as areas and edge lengths of a 2D Voronoi diagram representing skin scales.

For the case of skin scales arranged in a regular hexagonal lattice with side length $L_{kk'} = S$ for nearest-neighbor pairs, and corresponding hexagon area $A_k = 3\sqrt{3}S^2/2$, we obtain the result of Ref. [24]:

$$\frac{d}{dt}U_n^{(k)} = F_n(U_1^{(k)}, U_2^{(k)}, \ldots) + d_n \sum_{k'|k' \text{ NN of } k} (U_n^{(k')} - U_n^{(k)}), \quad (11)$$

where the sum is over nearest neighbors (NN), and $d_n = \alpha D_n$ is the effective diffusion coefficient of the dRD model with

$$\alpha = \frac{2P}{3\sqrt{3}S\epsilon} \quad (12)$$

being the effective diffusion reduction factor. The value of P is determined by the geometry of the bumps modeling the skin scales. For the bumps shown in Supplemental Material Fig. S3 [34], we have $S = 20/\sqrt{3}$ (in arb. units) and $P \approx 0.25$. Determining ϵ directly from the geometry is less easy. For bumps arranged in a hexagonal lattice with side S, the magnitude of the ratio ϵ/S is expected to be around the orders 10^{-1}–1, although it depends nontrivially on the geometry. Let us fix arbitrarily $\epsilon/S = 0.75$, which turns out to be adapted to the bump geometry used in Supplemental Material, Fig. S3 [34]. In this case, we find that $\alpha \approx 0.001$ for the conversion of the 3D cRD on this geometry to the relevant dRD. To probe how well the 3D cRD and the dRD match, the 3D cRD simulation on our geometry with bumps is compared with the corresponding dRD (Supplemental Material, Fig. S3C [34]). The reaction functions and the diffusion and interaction parameters are those used throughout most of main text to model ocellated lizard skin patterning, given in Eqs. (16) and (17) below. More realistic skin-scale geometries, inferred from microscopy data, can also be considered [25,33].

C. Implementations of the cRD and dRD models

Simulations of the 3D cRD system in Eq. (3) were performed using a standard finite element method with piecewise linear shape functions on a tetrahedral meshing of the spatial domain. The shape functions take the value 1 at a given vertex, and 0 on all the other vertices. We denote the vertex locations by $\mathbf{x}_i$ for $i = 1, \ldots, N_V$ and tetrahedra are defined by quadruplets $\mathbf{t}_k = (t_{k,1}, t_{k,2}, t_{k,3}, t_{k,4})$ for $k = 1, \ldots, N_E$; the kth quadruplet gives the label list of vertices forming the kth tetrahedron (k being the label of the tetrahedron). We also define the following set: K_{ij} is the list of labels of tetrahedra which have both vertices i and j as corners, then K_{ii} is the list of labels of all tetrahedra which have vertex i as a corner. The set K_{ij} is empty if i and j do not share an edge. Concentration values are defined on vertices $u_n^{(i)}(t) = u_n(\mathbf{x}_i, t)$ and the shape functions are used to interpolate between them inside the tetrahedra, and similarly for values of reaction functions $F_n^{(i)}(t) = F_n[u_1(\mathbf{x}_i, t), u_2(\mathbf{x}_i, t), \ldots]$ at a given time t. Projecting Eq. (3) on each of the shape functions (labeled also by $i = 1, \ldots, N_V$), we obtain the following ordinary differential equation system for $u_n^{(i)}(t)$:

$$\sum_j A_{ij}\dot{u}_n^{(j)}(t) = \sum_j \left(-B_{ij}^{(n)}u_n^{(j)}(t) + A_{ij}F_n^{(j)}(t)\right), \quad (13)$$

where

$$A_{ij} = \frac{\delta_{ij}+1}{20}\sum_{k\in K_{ij}} \mathcal{V}_k,$$
$$B_{ij}^{(n)} = \frac{1}{9}\sum_{k\in K_{ij}} \frac{\langle D_n\rangle_k}{\mathcal{V}_k}(\mathbf{n}_{i,k}\cdot\mathbf{n}_{j,k}). \quad (14)$$

In the above, $\mathcal{V}_k$ stands for the volume of the kth tetrahedron, $\mathbf{n}_{i,k}$ is the normal vector of the face in tetrahedron k opposite to vertex i (its norm being the area of that face), and $\langle D_n\rangle_k$ is the average value of $D_n(\mathbf{x})$ among the four vertices of tetrahedron k. In our case $D_n(\mathbf{x})$ is a constant function in space.

The time discretization of the above ordinary differential equation system is performed in a "mixed Euler scheme": the part coming from the diffusion and linear contributions

to the reaction are treated "backward" and the part coming from the nonlinear contributions of the reaction functions is treated "forward" in time. This allows for more numerical stability for reasonable time step Δt than with a purely forward method. The resulting linear system is

$$\sum_j (A_{ij} + \Delta t B_{ij}^{(n)}) u_n^{(j)}(t+\Delta t) = u_n^{(i)}(t) + \Delta t \sum_j A_{ij} F_n^{(j)}(t). \tag{15}$$

At each time step, the reaction functions $F_n^{(j)}$ are evaluated using the concentration values of the previous time step, and the solution of the above linear system is approximated using a quasiminimal residual method [available as QMR() in the numerical computing environment MATLAB 9.5 from *MathWorks*]. For the 3D numerical simulations, $\Delta t = 0.5$ was used.

Simulations of the dRD system [Eq. (10) for general Voronoi tesselations and Eq. (11) for hexagonal lattices] were performed using a simple forward Euler scheme. The time step used was $\Delta t = 0.4$ for all dRD simulations, unless otherwise specified.

D. Specific RD models

The precise form of the RD model is the one given in Refs. [17,24,25]. In this model, three dynamical variables (or concentrations) $u(\mathbf{x}, t)$, $v(\mathbf{x}, t)$, $w(\mathbf{x}, t)$, with $\mathbf{x} \in \Omega \subset \mathbb{R}^3$, represent the densities of two short-range factors u and v (corresponding to melanophores and xanthophores, respectively) and a long-range factor w (activated by u and inhibited by v). The 3D cRD system of three coupled nonlinear partial differential equations is

$$\begin{aligned} \frac{\partial u}{\partial t} &= F_u(u,v,w) - c_u u + D_u \nabla^2 u, \\ \frac{\partial v}{\partial t} &= F_v(u,v,w) - c_v v + D_v \nabla^2 v, \\ \frac{\partial w}{\partial t} &= F_w(u,v,w) - c_w w + D_w \nabla^2 w, \end{aligned} \tag{16}$$

where c_u, c_v, and c_w are decay terms, and the remaining nonlinear parts of the reaction are given by $F_{u,v,w}$:

$$\begin{aligned} F_u(u,v,w) &= \min[\max(c_1 v + c_2 w + c_3, 0), F_u^{\max}], \\ F_v(u,v,w) &= \min[\max(c_4 u + c_5 v + c_6, 0), F_v^{\max}], \\ F_w(u,v,w) &= \min[\max(c_7 u + c_8 v + c_9, 0), F_w^{\max}]. \end{aligned} \tag{17}$$

The signs of the variables c_1, c_2, c_4, c_5, c_7, and c_8 are constrained by the cell interaction model [17,24]. Using Eq. (11), the dRD model on a hexagonal lattice is

$$\begin{aligned} \dot{U}^{(k)} &= F_u(U^{(k)}, V^{(k)}, W^{(k)}) - c_u U^{(k)} + d_u \sum_{k'|k' \text{ NN of } k} (U^{(k')} - U^{(k)}), \\ \dot{V}^{(k)} &= F_v(U^{(k)}, V^{(k)}, W^{(k)}) - c_v V^{(k)} + d_v \sum_{k'|k' \text{ NN of } k} (V^{(k')} - V^{(k)}), \\ \dot{W}^{(k)} &= F_w(U^{(k)}, V^{(k)}, W^{(k)}) - c_w W^{(k)} + d_W \sum_{k'|k' \text{ NN of } k} (W^{(k')} - W^{(k)}). \end{aligned} \tag{18}$$

The set of parameter values used in our dRD simulations is optimized (over the parameter set c_8, c_w, $d_u = d_v$, d_w, the others being fixed to the values in Ref. [24]) with a Bayesian procedure that finds the parameters giving patterns best matching (using an objective function based on the nearest-neighbor statistics [24]) those of the lizard individual TL66. The precise method for the optimization procedure follows Ref. [33]. The values obtained for the parameters are $c_1 = -0.04$, $c_2 = -0.056$, $c_3 = 0.382$, $c_4 = -0.05$, $c_5 = 0$, $c_6 = 0.25$, $c_7 = 0.016$, $c_8 = -0.0325$, $c_9 = 0.24$, $c_u = 0.02$, $c_v = 0.025$, $c_w = 0.058$, $d_u = d_v = 0.000\,125$, $d_w = 0.009$, $F_u^{\max} = F_v^{\max} = F_w^{\max} = 0.5$.

E. Hyperspectral imaging, calibration, and control measurements

Images were captured with a hyperspectral camera (FireflEXE S185, Cubert GmbH, Ulm, Germany) whose objective was aligned to the eyepiece of a microscope (M80, Leica Microsystems, Wetzlar, Germany) at 5× magnification with reflected illumination. The camera spectral range is 450–950 nm with a 4 nm spectral sampling of the wavelength λ, but we only used the 462–702 nm range characterized by high signal-to-noise ratio in this setup. Each hyperspectral image includes 2500 spectra (i.e., the spatial resolution is 50×50 pixels). For each selected scale on the skin sample, the mean relative reflectance was computed (from the corresponding hyperspectral image) as the average among the approximately 40 pixels covering the central 30% of the scale (with the field of view including the full skin scale and its nearest neighbors). Reflectance was calibrated with a white plate provided by the camera manufacturer.

To ensure that neighborhood-dependent color subclustering was not due to trivial artifacts of measurements,

we performed a control experiment. The control sample used was a black and white printout of a dRD steady-state pattern (Supplemental Material, Fig. S16A [34]) where black scales are represented by black hexagons and green scales by "transparent" hexagons (i.e., the background whiteness of the extra-white paper used for the printing). Hexagons have the typical size of a lizard skin scale (i.e., a diameter of around 1 mm). The hyperspectral measurements and subsequent analysis of this control "artificial two-colored lizard skin" was performed exactly in the same way as of the actual data. The results (Supplemental Material, Figs. S16B–S16D [34]) indicate that *no* neighborhood-dependent color clustering is present on this artificial dataset; i.e., the same whiteness of the paper is measured by the hyperspectral camera on all sampled white hexagons. This control measurement rules out measurement bias contributing to neighborhood-dependent subclustering; hence, the intrinsic variation in the control dataset (Supplemental Material, Fig. S16C [34]) is interpreted as intrinsic measurement noise.

F. PCA and dimensional reduction of hyperspectral data

Dimensional reduction using principal component analysis was performed as follows (see, e.g., Ref. [46]). The corrected reflectance data are given by $\mathbf{r}_i = (r_{\lambda=462\ \mathrm{nm},i}, r_{\lambda=464\ \mathrm{nm},i}, \ldots, r_{\lambda=702\ \mathrm{nm},i}) \in \mathbb{R}^{61}$ for $i = 1, \ldots, N_{\mathrm{scales}}$, with sample mean

$$\bar{\mathbf{r}} = \frac{1}{N_{\mathrm{scales}}} \sum_{i=1}^{N_{\mathrm{scales}}} \mathbf{r}_i \tag{19}$$

and (unbiased) sample covariance matrix

$$\Sigma_{\mathbf{r}} = \frac{1}{N_{\mathrm{scales}} - 1} \sum_{i=1}^{N_{\mathrm{scales}}} (\mathbf{r}_i - \bar{\mathbf{r}})(\mathbf{r}_i - \bar{\mathbf{r}})^T. \tag{20}$$

Principal component analysis relies on decomposing the reduced data $\hat{\mathbf{r}}_i = \mathbf{r}_i - \bar{\mathbf{r}}$ (deviation from the mean) into orthogonal "modes" (principal directions). The first mode corresponds to the direction on which the projected data have the largest possible variance σ^2. The second corresponds to the direction orthogonal to the first mode on which the projected data have the second largest variance, and so on. These modes are given by the eigenvectors $\mathbf{v}_k$ of the sample covariance matrix $\Sigma_{\mathbf{r}}$ (symmetric, positive semidefinite): $\Sigma_{\mathbf{r}}\mathbf{v}_k = \sigma_k^2 \mathbf{v}_k$, where $\mathbf{v}_k^T \mathbf{v}_{k'} = \delta_{kk'}$. We order them according to decreasing values of the corresponding real non-negative eigenvalues $\sigma_1^2 \geq \sigma_2^2 \geq \cdots \geq \sigma_{61}^2$. Projection of a data point on a principal direction gives the value for its principal component for that principal direction: $c_i^{(k)} = \mathbf{v}_k^T \hat{\mathbf{r}}_i$. It has vanishing mean and (unbiased) variance given by the eigenvalue:

$$\begin{aligned} \frac{1}{N_{\mathrm{scales}} - 1} \sum_{i=1}^{N_{\mathrm{scales}}} (c_i^{(k)})^2 &= \frac{1}{N_{\mathrm{scales}} - 1} \mathbf{v}_k^T \left(\sum_{i=1}^{N_{\mathrm{scales}}} \hat{\mathbf{r}}_i \hat{\mathbf{r}}_i^T \right) \mathbf{v}_k \\ &= \mathbf{v}_k^T \Sigma_{\mathbf{r}} \mathbf{v}_k = \sigma_k^2. \end{aligned} \tag{21}$$

By construction, the different principal components are uncorrelated:

$$\sum_{i=1}^{N_{\mathrm{scales}}} c_i^{(k)} c_i^{(k')} = \mathbf{v}_{k'}^T \Sigma_{\mathbf{r}} \mathbf{v}_k = \sigma_k^2 \mathbf{v}_{k'}^T \mathbf{v}_k = 0 \quad (k \neq k'). \tag{22}$$

The sum of all the variances of the data is given by

$$\frac{1}{N_{\mathrm{scales}} - 1} \sum_{i=1}^{N_{\mathrm{scales}}} \hat{\mathbf{r}}_i^T \hat{\mathbf{r}}_i = \mathrm{tr}(\Sigma_{\mathbf{r}}) = \sum_{k=1}^{d} \sigma_k^2, \tag{23}$$

and the fraction of variance given by the kth mode is $\sigma_k^2 / \sum_{k'} \sigma_{k'}^2$.

Dimensional reduction using PCA consists in projecting out low variance modes, that is, approximating the data by its first few (high variance) principal components. For example, by only keeping the first two principal components, we replace the data

$$\mathbf{r}_i = \bar{\mathbf{r}} + \hat{\mathbf{r}}_i = \bar{\mathbf{r}} + \sum_{k=1}^{d} c_i^{(k)} \mathbf{v}_k \tag{24}$$

by its approximation

$$\mathbf{r}_i \approx \bar{\mathbf{r}} + c_i^{(1)} \mathbf{v}_1 + c_i^{(2)} \mathbf{v}_2. \tag{25}$$

This allows us to approximately represent the data using less degrees of freedom: deviation from the mean is represented here as two values per data point. The approximation is more precise when the neglected principal components have a low fraction of variance. In the main text, we used the notation $c_i^{(\mathrm{PC}_k)}$ instead of $c_i^{(k)}$ and $\mathbf{v}^{(\mathrm{PC}_k)}$ instead of $\mathbf{v}_k$.

G. Fisher linear discriminant analysis of hyperspectral data

Standard Fisher linear discriminant analysis allows us to find the features of the spectrum which correlate most with the group labeling. These were performed as follows (see, e.g., Ref. [46]). The relative reflectance data $\mathbf{r}_i$ are partitioned into groups according to the nearest-neighbor configuration $n_G = 1, 2, 3, 4$ as $\mathbf{r}_{n_G,i}$ with $i = 1, \ldots, N_{n_G}$ (N_{n_G} is the number of data points in the group). The sample mean of each group is

$$\bar{\mathbf{r}}_{n_G} = \frac{1}{N_{n_G}} \sum_{i=1}^{N_{n_G}} \mathbf{r}_{n_G,i}. \tag{26}$$

We define the following quantities: the between-group unnormalized covariance matrix,

$$S_{\text{between}} = \sum_{n_G=1}^{4} N_{n_G}(\bar{\mathbf{r}}_{n_G} - \bar{\mathbf{r}})(\bar{\mathbf{r}}_{n_G} - \bar{\mathbf{r}})^T, \tag{27}$$

and the within-group unnormalized covariance matrix,

$$S_{\text{within}} = \sum_{n_G=1}^{4} \sum_{i=1}^{N_{n_G}} (\mathbf{r}_{n_G,i} - \bar{\mathbf{r}}_{n_G})(\mathbf{r}_{n_G,i} - \bar{\mathbf{r}}_{n_G})^T. \tag{28}$$

We take a projector $\mathbf{y}^T$ and consider the ratio of between-group variance in that direction over the within-group variance in that direction. The linear discriminant mode of Fisher is the direction which maximizes this ratio:

$$\mathbf{v}_{\text{FLD}} = \arg\max_{\mathbf{y}|\mathbf{y}^2=1} \frac{\mathbf{y}^T S_{\text{between}} \mathbf{y}}{\mathbf{y}^T S_{\text{within}} \mathbf{y}}. \tag{29}$$

If S_{within} has full rank, the solution of this maximization problem is given by the eigenvector of $S_{\text{within}}^{-1} S_{\text{between}}$ corresponding to the largest eigenvalue. Projection of the dataset on the direction $\mathbf{v}_{\text{FLD}}$ gives the best clustering of the groups. More precisely, since the above ratio is (proportional to) the F statistic for the one-dimensional dataset given by the chosen projection, this procedure finds the direction which gives the best F-test score when the data are projected on it.

In contrast to PCA, the linear discriminant component may be associated to a small proportion of the total variance. In addition, FLDA depends on the group assignment whereas PCA does not use group labels (i.e., it is only an *a posteriori* observation that group labels correlate well or not with the first PC). In our context, we use Fisher linear discriminant to compare the F statistic (or its associated p value) of the dataset projected to the first principal direction $\mathbf{v}_1$ (PC_1) to the best possible case (i.e., the F statistic of the dataset projected to $\mathbf{v}_{\text{FLD}}$).

H. Statistical analyses

Starting from correlation plots (between principal components or between chromatophore spatial distribution parameters), data points are grouped according to their number of green neighbors (n_G) and credibility ellipses are constructed using Bayesian analysis of the 2D point clouds for a bivariate normal distribution with flat prior for the mean and log-flat prior for the principal variances (see Appendix B 1 for more details). In Figs. 3(c), 3(e), 5(a), and 5(c) (as well as Supplemental Material Figs. S7, S8, and S16C [34]), the outer and inner ellipses correspond to credibility volumes with probability $p = 0.99$ and $p = 0.9$, respectively. When two outer ellipses do not overlap, the two groups of data have a posterior probability $p < 0.01^2 = 10^{-4}$ to be sampled from multivariate normal distributions with the same mean. Dashed ellipses correspond to credibility volumes with probability $p = 0.9$ for small samples.

Standard analysis of variance (F-test), testing the null hypothesis that the data from the different groups are sampled from distributions with the same mean, and pairwise Tukey-Kramer tests, testing if differences in PC components are significant for pairwise group comparisons, were performed as in Ref. [47]. Box plots are drawn as follows: the mean is indicated as a red horizontal bar, the blue box is the interquartile range, and the whiskers indicate the range of data excluding outliers. The latter (drawn as red crosses) are data points lying > 1.5 times the interquartile range away from bottom or top of the box.

I. Analysis of histological data

Dorsal skin was fixed overnight in 4% paraformaldehyde, then stored in 10% formalin. Target pieces of skin were then sampled and dehydrated in ethanol before embedding in paraffin blocks. Seven-micrometer microtome serial sections were deparaffinized and processed as described in Ref. [48] for hematoxylin and eosin staining. Stained sections were mounted with Ultrakitt (no. 3921, JT Baker) and imaged with a slide scanner (Pannoramic Midi, 3DHISTECH, Budapest, Hungary) at a spatial resolution of 0.23 μm/pixel. Blurry images and those corresponding to damaged, deformed, or folded sections were discarded to yield a high-quality set of 3845 images (mean = 94 sections/scale). Each image of each scale section was color segmented in the standard CIELAB color space (a uniformised coordinate space adapted to human perception) using a partition defined after manual selection of typical pixels corresponding to epidermis (red label), melanophores (black label), and iridophores (blue label), or none of the above (empty label). Identification of the epidermis as a continuous line required manual input in some sections. Scale lateral borders were manually identified by the presence of the typical interscale "hinge" region. We note that xanthophores could not be observed because yellow pigments either degraded or have been washed away during the slide preparation process.

Approximate volumetric 3D reconstruction of skin scales was performed using rigid transformation between overlapping melanophore and iridophore distributions in consecutive XZ color-segmented sections. As sections are 7 μm thick and were scanned at a spatial resolution of 0.23 μm/pixel, each labeled XZ pixel was transformed into a voxel of $(0.23 \times 0.23 \times 7)$ μm^3. The boundary of the scale was then identified by fitting algebraically an ellipse to the XY projection of the epidermis data and restricting the XYZ data to the voxels both situated below the epidermis and whose XY projection falls inside the central 25% of the scale. The voxel data were used to obtain the volume fractions, and distributions of distance to the epidermis, of melanophores and iridophores.

J. Simulation of dRD for parameter scans

The discrete reaction diffusion system [Eq. (18)] for each parameter set validated by the semianalytical method was numerically simulated on a periodic 32×16 hexagonal grid representing skin scales. A hybrid time discretization scheme was used, where the reaction part is evaluated using the Euler forward method, and the diffusion term is evaluated using the backward method. This allows us to take relatively large time step Δt without numerical instability problems that are common in diffusive systems simulated with the Euler forward method. Here $\Delta t = 1$ was used. The initial conditions were given by slight perturbations of the homogeneous steady state (hSS) [Eq. (A1)], where the perturbation at each hexagon was drawn independently from a normal distribution with standard deviation given by $0.1 \times$ hSS value. Simulation was stopped if the system reached a steady state, or after 15 000 time units. At the end of the simulation, black and green clusters were identified by comparing the concentration values of the simulation to semianalytical cluster values [solutions of Eq. (A14)]. The state was assigned to the state of the cluster which is the closest in UVW space. The green cluster was defined to be the cluster with larger value of V. Once states were assigned, the nearest-neighbor statistics were obtained by counting all the number of all the neighborhood configurations arising in the final pattern of the simulation.

K. Determining (un)natural nearest-neighbor statistics

The statistics are given as fractions $N_G(n_G)/N_{\text{tot}}$ and $N_B(n_B)/N_{\text{tot}}$, where $N_G(n_G)$ is the number of green hexagons with n_G green nearest neighbors, $N_B(n_B)$ is the number of black hexagons with n_B black nearest neighbors, and N_{tot} is the total number of hexagons representing skin scales. In the case of the numerical simulations, we have $N_{\text{tot}} = 32 \times 16 = 512$. In the case of the real lizard, we have $N_{\text{tot}} = 1508$ skin scales in our dataset (see Supplemental Material, Fig. S12 [34]). Confidence intervals for the ratios $N_{G,B}(n_{G,B})/N_{\text{tot}}$ were estimated by assuming that these values follow a binomial distribution with probability $f_{G,B}(n_{G,B})$ (considered to be the true nearest-neighbor statistics). With this assumption, Bayesian posterior probability with uniform prior can be obtained for $f_{G,B}(n_{G,B})$ in the standard way. This posterior probability, a beta distribution, has a mode given by $N_{G,B}(n_{G,B})/N_{\text{tot}}$, and mean and standard deviation given by

$$\mu_{f_G(n_G)} = \frac{N_G(n_G)+1}{N_{\text{tot}}+2},$$
$$\sigma_{f_G(n_G)} = \frac{[N_G(n_G)+1][N_{\text{tot}}-N_G(n_G)+1]}{(N_{\text{tot}}+2)^2(N_{\text{tot}}+3)}, \quad (30)$$

and similarly for the black distribution $f_B(n_B)$ with B replacing G. We used these values to define confidence intervals for the value of the nearest-neighbor statistics $f_{G,B}(n_{G,B})$ inferred from the data. For a given positive value a, the interval is

$$I_G(n_G;a) = [\mu_{f_G(n_G)} - a\sigma_{f_G(n_G)}, \mu_{f_G(n_G)} + a\sigma_{f_G(n_G)}], \quad (31)$$

and similarly for the black distribution.

In the present work, we compute these intervals for the lizard nearest-neighbor data (Supplemental Material, Fig. S12A [34]), and define that parameters with good nearest-neighbor statistics are those whose simulated nearest-neighbor statistics $N_{G,B}(n_{G,B})/N_{\text{tot}}$ fall within the interval $I_{G,B}(n_{G,B};a)$ given by the lizard data for all $n_{G,B} = 0, 1, \ldots, 6$ for both green and black scales. We fix $a = 10$ (Supplemental Material, Fig. S12B [34]). More stringent cases were obtained for smaller values of a (Supplemental Material, Fig. S14 [34]).

L. Determining blackness correlation direction for green scales in simulations

In all valid simulations, we have determined the states of the hexagons by identifying the main clusters $\mathbf{U}^{(G)} = (U^{(G)}, V^{(G)}, B^{(G)})$ and $\mathbf{U}^{(B)} = (U^{(B)}, V^{(B)}, B^{(B)})$. The UVW values subcluster into smaller groups according to their nearest-neighbor configurations, with average UVW values given by $\mathbf{U}^{(G,n_G)}$ and $\mathbf{U}^{(B,n_B)}$ (also three-vectors), determined from the simulations. The blackness correlation of the green scales is fixed by looking at the U-component (= melanophore factor) difference of subcluster averages. More precisely, we consider the two extremes:

$$\delta U^{(G)}_{\min} = \min_{n_G}(U^{(G,n_G)} - U^{(G,n_G-1)}),$$
$$\delta U^{(G)}_{\max} = \max_{n_G}(U^{(G,n_G)} - U^{(G,n_G-1)}), \quad (32)$$

and the average,

$$\delta U^{(G)} = \frac{1}{6}\sum_{n_G=1}^{6}(U^{(G,n_G)} - U^{(G,n_G-1)}) = \frac{U^{(G,6)} - U^{(G,0)}}{6}. \quad (33)$$

The relative correlations (and their minimum and maximum) are obtained by dividing these values by the difference of main clusters:

$$\delta U^{(G,\text{rel})} = \frac{\delta U^{(G)}}{|U^{(G)} - U^{(B)}|},$$
$$\delta U^{(G,\text{rel})}_{\min,\max} = \frac{\delta U^{(G)}_{\min,\max}}{|U^{(G)} - U^{(B)}|}. \quad (34)$$

We can define the same quantities for V (xanthophore factor) and W (long-range factor). The correct blackness

correlation directions, i.e., correlations which are consistent with experimental observations from hyperspectral measurements and chromatophore content, are determined by the numerical condition:

$$\delta U_{\min}^{(G,\mathrm{rel})} > 10^{-6}. \tag{35}$$

The incorrect blackness correlation directions, i.e., correlations which are inconsistent with experimental observations and measurements, are determined by the numerical condition:

$$\delta U_{\max}^{(G,\mathrm{rel})} < -10^{-6}. \tag{36}$$

Otherwise, the correlation condition is considered to be undetermined.

ACKNOWLEDGMENTS

We thank Ebrahim Jahanbakhsh for performing the Bayesian optimization of RD parameters and commenting on technical aspects of simulations and dRD derivation. We thank Adrien Debry and Florent Montange for technical assistance with animals, Valérie Haechler and Athanasia Tzika for assistance with histology. This work was supported by grants to MCM from the Georges and Antoine CLARAZ foundation, the Swiss National Science Foundation (FNSNF, Grants No. 31003A_179431 and No. CR32I3), the International Human Frontier Science Program Organisation (HFSP RGP0019/2017), and the European Research Council (ERC, Advanced Grant EVOMORPHYS) under the European Union's Horizon 2020 research and innovation programme.

The funding bodies played no role in the design of the study, collection, analysis, and interpretation of data and in writing the paper. The authors declare no competing interests.

APPENDIX A: SUPPLEMENTAL ANALYTICAL INVESTIGATION OF THE dRD

1. Linear stability analysis and Turing length

The linear stability analysis for the discrete reaction-diffusion system in Eq. (18) is standard, and is similar to the analysis for the equivalent continuous model. A homogeneous steady state $(U^{(k)}, V^{(k)}, W^{(k)}) \equiv (U^*, V^*, W^*)$ for the RD system satisfies (in vector-matrix notation)

$$\begin{pmatrix} 0 \\ 0 \\ 0 \end{pmatrix} = \begin{pmatrix} F_u(U^*, V^*, W^*) - c_u U^* \\ F_v(U^*, V^*, W^*) - c_v V^* \\ F_w(U^*, V^*, W^*) - c_w W^* \end{pmatrix}. \tag{A1}$$

For the coefficients given in Sec. VI D, the solution of interest is $(U^*, V^*, W^*) \approx (3.52, 2.96, 3.45)$. In the absence of diffusion, this steady state is stable, while it may become unstable when diffusion is present. To investigate the behavior of the system, it is standard to decompose small perturbations around the homogeneous steady state into linearly independent spatial modes of the Laplacian operator [which, in the discrete case, is the sums over nearest neighbors in Eq. (18)]. The spatial modes are labeled by a wave number $\kappa \geq 0$, such that the spatial mode $f_\kappa^{(k)}$ satisfies

$$\sum_{k'|k' \text{ NN of } k} (f_\kappa^{(k')} - f_\kappa^{(k)}) = -\kappa^2 f^{(k)}, \tag{A2}$$

i.e., is an eigenmode of the discrete Laplacian operator. The typical length scale (in length unit given by the spatial discretization, i.e., the distance between two hexagons) of the spatial variation of a mode with wave number κ is $2\pi/\kappa$, in analogy with the decomposition in Fourier modes. For the particular case $\kappa = 0$, the eigenmode is the spatially constant function. The decomposition of the concentration perturbations is then

$$\begin{pmatrix} U^{(k)} \\ V^{(k)} \\ W^{(k)} \end{pmatrix} = \begin{pmatrix} U^* \\ V^* \\ W^* \end{pmatrix} + \sum_\kappa \begin{pmatrix} U_\kappa \\ V_\kappa \\ W_\kappa \end{pmatrix} f_\kappa^{(k)}. \tag{A3}$$

The U_κ, V_κ, W_κ are the mode amplitudes, which we assume to be small. Injecting this decomposition into Eq. (18) and linearizing for small mode amplitudes, we get the following system of ordinary differential equations for the spatial modes:

$$\begin{pmatrix} \dot{U}_\kappa \\ \dot{V}_\kappa \\ \dot{W}_\kappa \end{pmatrix} = [M_F - \kappa^2 M_D] \begin{pmatrix} U_\kappa \\ V_\kappa \\ W_\kappa \end{pmatrix}, \tag{A4}$$

where

$$M_F = \begin{pmatrix} \partial_u F_u - c_u & \partial_v F_u & \partial_w F_u \\ \partial_u F_v & \partial_v F_v - c_v & \partial_w F_v \\ \partial_u F_w & \partial_v F_w & \partial_w F_w - c_w \end{pmatrix},$$
$$M_D = \begin{pmatrix} d_u & 0 & 0 \\ 0 & d_v & 0 \\ 0 & 0 & d_w \end{pmatrix}. \tag{A5}$$

The entries of the matrix M_F are to be evaluated at the homogeneous steady state. In our case, these are linear functions of $c_{1,\ldots,9,u,v,w}$. An autonomous linear system, such as the one above, can be solved by matrix exponentiation. Equivalently, we can identify the three linearly independent eigenvectors $\mathbf{v}_i(\kappa)$ of the time-independent matrix $[M_F - \kappa^2 M_D]$, with eigenvalue $\lambda_i(\kappa)$ for $i = 1, 2, 3$, and decompose

$$\begin{pmatrix} U_\kappa \\ V_\kappa \\ W_\kappa \end{pmatrix} = \sum_i c_i \mathbf{v}_i(\kappa). \tag{A6}$$

For each eigenvector, we get the ordinary differential equation $\dot{c}_i = \lambda_i(\kappa) c_i$, which is solved as

$$c_i(t) = c_i(0) \exp[\lambda(\kappa) t]. \tag{A7}$$

The eigenvalues are found using the algebraic relation $\det[M_F - \kappa^2 M_D - \lambda I] = 0$. The solution for the linearized system is then

$$\begin{pmatrix} U^{(k)} \\ V^{(k)} \\ W^{(k)} \end{pmatrix} = \begin{pmatrix} U^* \\ V^* \\ W^* \end{pmatrix} + \sum_{\kappa,i} c_i(0) \mathbf{v}_i(\kappa) f_\kappa^{(k)} c_i(0) \exp[\lambda(\kappa) t]. \tag{A8}$$

Spatial modes with wave number κ for which at least one of the eigenvalues $\lambda_i(\kappa^2)$ satisfies $\mathrm{Re}]\lambda_i(\kappa^2)] > 0$ are linearly unstable. If such modes exist, it is said that the homogeneous steady state has a diffusion instability (or "Turing instability"). In many nonlinear systems, these growing modes are stabilized into stable inhomogeneous states through the nonlinearities of the system. The wave number κ_T which maximizes $\mathrm{Re}[\lambda_i(\kappa^2)]$ gives the fastest growing mode, which may give an estimate $L_T \approx 2\pi/\kappa_T$ for the typical length scale L_T (or "Turing length scale") of the stable patterns, at least in simple models as this one. For the RD parameter values given in the main text, we show the functions $\mathrm{Re}[\lambda_{1,2,3}(\kappa^2)]$ in the Supplemental Material, Fig. S17 [34]. The maximum is attained by $\lambda_1(\kappa^2)$ at $\kappa \approx 5.40$, giving a typical length scale of $L_T \approx 1.16$ (in spatial units given by the hexagonal lattice spacing $= \sqrt{3}S$).

2. Values of subclusters in concentration space can be analytically approximated

On a perfect hexagonal lattice, the steady-state solution of the dRD system exhibits clustering of final values of concentrations (interpreted as green and black scales) as well as subclustering of each of these clusters according to nearest-neighbor configuration (the number of isochromatic nearest neighbors). We present here an analytical procedure to approximate the location of these (sub)clusters in UVW concentration space. We start with the dRD of Eq. (18) on a perfect hexagonal lattice, and consider the time evolution of the concentration (U, V, W) of a single hexagon in a fixed neighborhood (with k' labeling the nearest neighbors):

$$\begin{aligned} \dot{U} &= F_u(U,V,W) - c_u U + d_u \sum_{k'=1}^{6} (U^{(k')} - U), \\ \dot{V} &= F_v(U,V,W) - c_v V + d_v \sum_{k'=1}^{6} (V^{(k')} - V), \\ \dot{W} &= F_w(U,V,W) - c_w W + d_w \sum_{k'=1}^{6} (W^{(k')} - W), \end{aligned} \tag{A9}$$

where $d_{u,v,w} = 2PD_{u,v,w}/(3\sqrt{3}S\epsilon)$ are the reduced effective diffusion constants of the dRD. It will be convenient to use vector-matrix notation:

$$\dot{\mathbf{U}} = \mathbf{F}(\mathbf{U}) + M_D \sum_{k'=1}^{6} (\mathbf{U}^{(k')} - \mathbf{U}), \tag{A10}$$

where

$$\mathbf{U} = \begin{pmatrix} U \\ V \\ W \end{pmatrix}, \qquad \mathbf{F}(\mathbf{U}) = \begin{pmatrix} F_u(U,V,W) - c_u U \\ F_v(U,V,W) - c_v V \\ F_w(U,V,W) - c_w W \end{pmatrix},$$
$$M_D = \begin{pmatrix} d_u & 0 & 0 \\ 0 & d_v & 0 \\ 0 & 0 & d_w \end{pmatrix}. \tag{A11}$$

(a) *Main clusters*. We want to find approximate values for the green state $\mathbf{U}^{(G)} = (U^{(G)}\, V^{(G)}\, W^{(G)})^T$ and the black state $\mathbf{U}^{(B)} = (U^{(B)}\, V^{(B)}\, W^{(B)})^T$. We denote the typical number of green nearest neighbors of a green hexagon by $\bar{n}_G$, and the typical number of black nearest neighbors of a black hexagon by $\bar{n}_B$. In the presence of these typical fixed nearest-neighbor configurations, the time dynamics of a green hexagon is

$$\dot{\mathbf{U}} = \mathbf{F}(\mathbf{U}) - 6M_D\mathbf{U} + \bar{n}_G M_D \mathbf{U}^{(G)} + (6 - \bar{n}_G) M_D \mathbf{U}^{(B)}, \tag{A12}$$

since we assume that the nearest neighbors already attained the green or black state. Similarly, a black hexagon's time dynamics is

$$\dot{\mathbf{U}} = \mathbf{F}(\mathbf{U}) - 6M_D\mathbf{U} + \bar{n}_B M_D \mathbf{U}^{(B)} + (6 - \bar{n}_B) M_D \mathbf{U}^{(G)}. \tag{A13}$$

By consistency, the states $\mathbf{U}^{(G)}$ and $\mathbf{U}^{(B)}$ should be stable steady states of Eqs. (A12) and (A13), respectively. This consistency condition leads to the following system corresponding to 6 equations for the 6 unknowns $(U^{(G)}, V^{(G)}, W^{(G)}, U^{(B)}, V^{(B)}, W^{(B)})$:

$$0 = \mathbf{F}(\mathbf{U}^{(G)}) - (6-\bar{n}_G)M_D(\mathbf{U}^{(G)} - \mathbf{U}^{(B)}),$$
$$0 = \mathbf{F}(\mathbf{U}^{(B)}) - (6-\bar{n}_B)M_D(\mathbf{U}^{(B)} - \mathbf{U}^{(G)}). \quad \text{(A14)}$$

This can be solved numerically, or even exactly in the case where the $F_{u,v,w}$ are piecewise-linear functions. The solutions $\mathbf{U}^{(G)} = (U^{(G)}\, V^{(G)}\, W^{(G)})^T$ and $\mathbf{U}^{(B)} = (U^{(B)}\, V^{(B)}\, W^{(B)})^T$ are interpreted (if stable fixed points) as the approximated locations of the green and black clusters, respectively. We usually fix $\bar{n}_G = 2$ and $\bar{n}_B = 3$.

(b) *Subclusters.* Now that the values for the main clusters are determined, we can look for the subcluster values by changing the number $n_G = 0, 1, \ldots, 6$ of nearest neighbors in the green state. We fix the $\mathbf{U}^{(k')}$ values of the nearest neighbors in Eq. (A10) using the approximation $\mathbf{U}^{(G,B)}$ obtained from Eq. (A14). The central hexagon has time evolution

$$\dot{\mathbf{U}} = \mathbf{F}(\mathbf{U}) - 6M_D\mathbf{U} + n_G M_D\mathbf{U}^{(G)} + (6-n_G)M_D\mathbf{U}^{(B)}, \quad \text{(A15)}$$

and its steady-state value is obtained by setting $\dot{\mathbf{U}} = 0$. Again, this can be solved numerically, or even exactly in the piecewise-linear case. The solutions close to the green cluster $\mathbf{U}^{(G)}$ give the approximate subcluster positions $\mathbf{U}^{(G,n_G)}$ and those close to the black cluster $\mathbf{U}^{(B)}$ give the approximate subcluster positions $\mathbf{U}^{(B,n_B)}$ (where $n_B = 6 - n_G$), although we have to check their stability. We note that $\mathbf{U}^{(G,n_G=\bar{n}_G)} = \mathbf{U}^{(G)}$ and $\mathbf{U}^{(G,n_B=\bar{n}_B)} = \mathbf{U}^{(B)}$ because of Eq. (A14). We can linearize the reaction function $\mathbf{F}(\mathbf{U})$ around $\mathbf{U}^{(G,B)}$:

$$\mathbf{F}(\mathbf{U}) = \mathbf{F}(\mathbf{U}^{(G)}) + M_F^{(G)}(\mathbf{U} - \mathbf{U}^{(G)}) + \cdots$$
$$= \mathbf{F}(\mathbf{U}^{(B)}) + M_F^{(B)}(\mathbf{U} - \mathbf{U}^{(B)}) + \cdots, \quad \text{(A16)}$$

where $M_F^{(G,B)}$ are the matrices giving the linear approximations of the reaction function close to the green and black clusters. For piecewise-linear reaction functions, these expansions are locally exact. Using these expansions, the linearized dynamical system for small deviations from the green state $\delta\mathbf{U} = \mathbf{U} - \mathbf{U}^{(G)}$ can be written as

$$\delta\dot{\mathbf{U}} = (M_F^{(G)} - 6M_D)\delta\mathbf{U} + (n_G - \bar{n}_G)M_D(\mathbf{U}^{(G)} - \mathbf{U}^{(B)}), \quad \text{(A17)}$$

and similarly for the small deviations from the black state:

$$\delta\dot{\mathbf{U}} = (M_F^{(B)} - 6M_D)\delta\mathbf{U} - (n_B - \bar{n}_B)M_D(\mathbf{U}^{(G)} - \mathbf{U}^{(B)}). \quad \text{(A18)}$$

It is therefore clear that the local shape of the reaction function $M_F^{(G,B)}$ and the concentration difference between the two main clusters $(\mathbf{U}^{(G)} - \mathbf{U}^{(B)})$ strongly influence the direction of correlation of subclusters with nearest-neighbor configurations. In addition, for the subclusters to be stable, the eigenvalues of the matrices $(M_F^{(G)} - 6M_D)$ and $(M_F^{(B)} - 6M_D)$ should all have negative real part. In particular, this implies that the direction of correlation for the green subclusters $\delta\mathbf{U}^{(G)}$, which is the solution of Eq. (A17) for $\delta\dot{\mathbf{U}} = 0$ and $(n_G - \bar{n}_G) = 1$, i.e.,

$$(M_F^{(G)} - 6M_D)\delta\mathbf{U}^{(G)} = -M_D(\mathbf{U}^{(G)} - \mathbf{U}^{(B)}), \quad \text{(A19)}$$

cannot be a positive multiple of the vector $M_D(\mathbf{U}^{(B)} - \mathbf{U}^{(G)})$. Indeed, if it were the case, then $M_D(\mathbf{U}^{(B)} - \mathbf{U}^{(G)})$ would be an eigenvector of $(M_F^{(G)} - 6M_D)$ with a strictly positive eigenvalue, but this would contradict the stability of the subclusters which requires that all eigenvalues of $(M_F^{(G)} - 6M_D)$ have negative real parts. Therefore, $\delta\mathbf{U}^{(G)}$ and $M_D(\mathbf{U}^{(B)} - \mathbf{U}^{(G)})$ will point in different directions. In the case where all the eigenvalues of $(M_F^{(G)} - 6M_D)$ (and therefore of its inverse) are strictly negative (i.e., have no imaginary part) [49], the allowed wedge containing $\delta\mathbf{U}^{(G)}$ is simply constructed: it is the wedge which is the octant (or more generally the orthant, i.e., quadrant for two concentration models, octant for three concentration models, etc.) in the eigenbasis of $(M_F^{(G)} - 6M_D)$ lying opposite to the one containing $M_D(\mathbf{U}^{(B)} - \mathbf{U}^{(G)})$; see Supplemental Material Fig. S18 [34] for a sketch. The case of the black cluster is similar. We showed here that the correlation direction of subclusters is linked to local stability of color states.

(c) *Subclusters for mildly heterogeneous edge lengths.* In the case were the hexagonal geometry is slightly perturbed so that edge lengths are distributed around their typical value S, we can incorporate this effect in the computation of the approximation of the location of the subclusters by using Eq. (10) [instead of Eq. (11)] for a single hexagon with fixed neighbors:

$$\dot{\mathbf{U}} = \mathbf{F}(\mathbf{U}) + \frac{P}{A_k\epsilon}D\sum_{k'=1}^{6} L_{kk'}(\mathbf{U}^{(k')} - \mathbf{U})$$
$$= \mathbf{F}(\mathbf{U}) + \frac{P}{A_k\epsilon}D\left(\mathcal{L}_k\mathbf{U}^{(G)} + (\mathcal{L}_k - \mathcal{L}_k^{\text{tot}})\mathbf{U}^{(B)} - \mathcal{L}_k^{\text{tot}}\mathbf{U}\right), \quad \text{(A20)}$$

where D is now the diagonal matrix of 3D diffusions $D_{u,v,w}$,

$$\mathcal{L}_k = \sum_{k'} \delta_{s_k s_{k'}} L_{kk'} \qquad \text{where } s_k = \begin{cases} 1 & \text{if } k \text{ green} \\ 0 & \text{if } k \text{ black} \end{cases} \tag{A21}$$

and

$$\mathcal{L}_k^{\text{tot}} = \sum_{k'} L_{kk'}. \tag{A22}$$

The steady-state solutions of Eq. (A20) give the subcluster positions. The solutions close to the green cluster $\mathbf{U}^{(G)}$ give the approximate subcluster positions $\mathbf{U}^{(G,\mathcal{L}_k)}$ which now depends on $\mathcal{L}_k$ instead of n_G. Note that we recover the previous construction by setting $\mathcal{L}_k = n_G S$ and $\mathcal{L}_k^{\text{tot}} = 6S$. The same can be done for black subclusters.

3. Effect of skin-scale size on subclustering

Although the correlation between the U and V values of a scale and the color of its nearest neighbors is always maintained, the resulting subclusters in the discrete model tend to merge as the size of scales becomes smaller (Supplemental Material, Fig. S19 [34]). Further reduction of scale size even leads to the merger of the two main (green and black) clusters such that a continuum of possible stable colors between black and green is observed (Supplemental Material, Fig. S19C [34]).

APPENDIX B: SUPPLEMENTAL METHODS

1. Construction of credibility ellipses

The data of a given group are denoted by $\mathbf{x}_i \in \mathbb{R}^d$, with $i = 1, \ldots, N$ (N is the number of data points in that group, and d is the dimensionality of the data; i.e., $d = 2$ in our applications). It is assumed to be an independent sampling of a multivariate Gaussian distribution (one for each group) with mean parameter $\mathbf{m}$ and covariance matrix parameter Σ (a positive-definite symmetric matrix). The probability density to draw the data is

$$f(\mathbf{x}_1, \ldots, \mathbf{x}_N | \mathbf{m}, \Sigma) = \frac{1}{|2\pi\Sigma|^{N/2}} \exp\left(-\frac{1}{2} \sum_i (\mathbf{x}_i - \mathbf{m})^T \Sigma^{-1} (\mathbf{x}_i - \mathbf{m}) \right). \tag{B1}$$

Using Bayes's formula, we get the conditional probability for the parameters given the observed data:

$$f(\mathbf{m}, \Sigma | \mathbf{x}_1, \ldots, \mathbf{x}_N) = \frac{f(\mathbf{x}_1, \ldots, \mathbf{x}_N | \mathbf{m}, \Sigma) f(\mathbf{m}, \Sigma)}{\int d^d m d^{d(d+1)/2} \Sigma f(\mathbf{x}_1, \ldots, \mathbf{x}_N | \mathbf{m}, \Sigma) f(\mathbf{m}, \Sigma)}. \tag{B2}$$

Choosing a prior $f(\mathbf{m}, \Sigma)$ which is "flat" for $\mathbf{m}$ and a "log-flat" ($\propto |\Sigma|^{(d+1)/2}$) for Σ (both unnormalizable, the former is symmetric under translation, the latter is symmetric under inversion), we have, up to a normalizing factor,

$$f(\mathbf{m}, \Sigma | \mathbf{x}_1, \ldots, \mathbf{x}_N) \propto \frac{1}{|\Sigma|^{(N+d+1)/2}} \exp\left(-\frac{1}{2} \sum_i (\mathbf{x}_i - \mathbf{m})^T \Sigma^{-1} (\mathbf{x}_i - \mathbf{m}) \right). \tag{B3}$$

After marginalizing, i.e., integrating out the covariance parameter matrix Σ, it can be shown that the marginal density for the mean parameter is, up to a constant,

$$f(\mathbf{m} | \mathbf{x}_1, \ldots, \mathbf{x}_N) \propto \left(1 + \frac{N}{N-1} (\mathbf{m} - \bar{\mathbf{x}})^T \Sigma_{\mathbf{x}} (\mathbf{m} - \bar{\mathbf{x}}) \right)^{-N/2}, \tag{B4}$$

where $\bar{\mathbf{x}}$ is the sample mean, and $\Sigma_{\mathbf{x}}$ is the (unbiased) sample covariance matrix for $\mathbf{x}_i$. This probability distance can be expressed using the t-squared variable (or t-squared statistic):

$$t_2 = N(\mathbf{m} - \bar{\mathbf{x}})^T \Sigma_{\mathbf{x}}^{-1} (\mathbf{m} - \bar{\mathbf{x}}). \tag{B5}$$

The probability density for t_2 is given by

$$f(t_2) = \frac{1}{(N-1)^{d/2} \mathrm{B}\left(\frac{N-d}{2}, \frac{d}{2}\right)} t_2^{d/2-1} \left(1 + \frac{1}{N-1} t_2 \right)^{-N/2}, \tag{B6}$$

which is precisely the Hotelling t-squared distribution [50] (B is the Euler beta function). A Bayesian credibility ellipse associated to probability p is the region of constant $t_2 = T_2$ inside which we can find the parameter $\mathbf{m}$ with probability p. To build it, we use that

$$p = \int_0^{T_2} f(t_2) dt_2 = 1 - \mathcal{I}_{N-d/2,\, d/2}\left(\frac{1}{1 + \frac{1}{N-1} T_2} \right), \tag{B7}$$

where $\mathcal{I}_{a,b}(z)$ is the regularized incomplete beta function. For fixed p, the corresponding value of T_2 is found by inverting this relation, giving

$$T_2 = (N_{n_G} - 1) \left(\frac{1}{\mathcal{I}^{-1}_{N-d/2,\, d/2}(1-p)} - 1 \right). \tag{B8}$$

The inverse of the regularized incomplete beta function can be evaluated (e.g., it is numerically implemented in the computing environment MATLAB 9.5 from *MathWorks*). Once T_2 is computed, the ellipse can be constructed by using its implicit definition above; that is, $T_2 = N(\mathbf{m} - \bar{\mathbf{x}})^T \Sigma_{\mathbf{x}}^{-1} (\mathbf{m} - \bar{\mathbf{x}})$.

For example, one can use the parametrization of a unit d sphere $\mathbf{r}(\Omega)$, and perform the transformation

$$\sqrt{\frac{T_2}{N}}R\Lambda^{1/2}\mathbf{r}(\Omega)+\bar{\mathbf{x}}, \tag{B9}$$

where R, Λ are given by the eigendecomposition of the sample covariant matrix $\Sigma_{\mathbf{x}}=R\Lambda R^T$.

APPENDIX C: SUPPLEMENTARY RESULTS ON SUBCLUSTERING CORRELATION ORIENTATION

1. Different RD models produce different neighborhood-dependent subclustering orientations

We have shown that neighborhood-dependent subclustering of component concentrations is a generic feature of RD models, irrespective of their form, discretization, and projection in lower spatial dimensions. This observation makes intuitive sense as it is logically coherent with the principles of RD: the local state of the system (here, the color of a scale) is influenced by its neighborhood (here, the colors of neighbor scales) through diffusion. However, we additionally show here that the observed correlation can, counterintuitively, take different "orientations" (in RD-components space) depending on the model and its parameters. Let us take, for example, two models with only two components (Supplemental Material, Fig. S4 [34]): the Gray-Scott model [36,37],

$$\begin{aligned}\frac{\partial u}{\partial t}&=D_u\nabla^2u+[-uv^2+a(1-u)],\\ \frac{\partial v}{\partial t}&=D_v\nabla^2v+(uv^2-bv),\end{aligned} \tag{C1}$$

and the Gierer-Meinhardt model [3],

$$\begin{aligned}\frac{\partial u}{\partial t}&=D_u\nabla^2u+\left(a-bu+\frac{u^2}{v}\right),\\ \frac{\partial v}{\partial t}&=D_v\nabla^2v+(u^2-v).\end{aligned} \tag{C2}$$

Using the Gray-Scott model and arbitrarily deciding that the concentrations of components U and V represent blackness and greenness, respectively, the correlation between the color of green scales and the number of green neighbors (n_G, i.e., neighbors belonging to the first-order cluster with high values of V) is positive for blackness and negative for greenness (Supplemental Material, Fig. S4C; bottom right-hand panel in left-hand column [34]). This subclustering correlation within the green cluster is in line with the antagonistic direct-neighbor interactions governing green-to-black scale color flipping. In other words, if a green scale tends to flip to black when surrounded by many green scales, it makes intuitive sense that scales that remain green still tend to become slightly more black and less green for larger number of green neighbors. However, this intuition breaks down for black scales (Supplemental Material, Fig. S4, bottom left-hand panel [34]): the correlation between the color of black scales and the number of black neighbors (n_B, i.e., neighbors belonging to the first-order cluster with high values of U) is also positive for blackness and negative for greenness; i.e., scales that remain black tend to become slightly *more* black and *less* green for larger number of black neighbors, despite that a black scale with many black neighbors tends to flip to green. Note that this result is not due to the arbitrary decision of considering U and V as the black and green components, respectively. Indeed, when making the reverse choice, the subclustering correlation in the black cluster (now corresponding to high values of V) conforms with the black-to-green flipping process, but the subclustering correlation in the green cluster (now corresponding to high values of U) takes an orientation that is unintuitive in comparison to the green-to-black color flipping process.

When using the Gierer-Meinhardt model (Supplemental Material, Fig. S4, middle column [34]), the decrease of green-scale blackness with an increase in the number of green neighbors is at odds with green-to-black flipping, but the decrease of black-scale blackness with an increase in the number of black neighbors is in line with the black-to-green flipping rules. Conversely, the influence of isochromatic neighbors on greenness is intuitive for green scales and unintuitive for black scales. Evidently, when considering relations among subclusters, the specific correlations between, on one hand, the greenness or blackness of scales and, on the other hand, the number of same-color neighbors, can take multiple orientations in RD-components space depending on the model. When using the single-component Allen-Cahn-type model,

$$\frac{\partial v}{\partial t}=D_v\nabla^2v-v(v-a)(v-b), \tag{C3}$$

the greenness of black scales decreases with the number of black neighbors and the greenness of green scales increases with the number of green neighbors (Supplemental Material, Fig. S4, right-hand column [34]), both observations being counterintuitive.

2. Different sets of parameter values within a RD model produce different neighborhood-dependent subclustering orientations

The Nakamasu-Takahashi-Kanbe-Kondo (NTKK-2009) three-component RD model [17] (see Sec. VI D), optimized here for the skin color patterning in ocellated lizards, generates the following relations [Fig. 1(e)]: a black scale is both less green (smaller value of V) and less black (smaller value of U) when the number of its black neighbors increases, whereas a green scale is greener

(higher value of V) and less black (smaller value of U) when the number of its green neighbors increases. Note that there is ambiguity in interpreting this latter relation in the context of the hyperspectral measurements and histological analyses (Figs. 3–5). Indeed, these experimental data indicate that green scales are darker when surrounded by larger numbers of green direct neighbors. However, a green scale can be measured as "darker" because of a decrease in V or an increase in U or both. We have shown in the main text (Fig. 6) that each of these two possibilities can be observed for different parameter values of the NTKK-2009 model while maintaining the correct dynamics of green-to-black and black-to-green color changes. In other words, we have shown that, counterintuitively, different sets of parameters *within* a given model can generate different (correct or incorrect) orientations of subclustering correlations.

The Fisher linear discriminant method did not manage to sharply partition the parameter space into two distinct regions (correct vs incorrect blackness correlation). However, such a sharp partition would be expected since the parameters completely specify the blackness correlation direction. This probably happens because the boundary does not lie on a hyperplane but a on a more complicated hypersurface. We tested a quadratic discriminant which slightly improved the distinction between the two regions, but made harder the interpretation in terms of model parameters. The fact that this boundary does not lie on a hyperplane means that the parameters that influence blackness correlation direction may depend on the values of the parameters themselves. It could be argued that, if this dependence is very strong, it reduces the interest of the effective dRD model for understanding the patterning mechanism in terms of interacting chromatophores, since, for example, the effects influencing blackness correlation identified above would not be general. In other words, the model would not provide informative constraints on chromatophore interaction when blackness correlation is taken into account. By scanning 10 small regions of parameter space close to this boundary (Supplemental Material, Fig. S15 [34]), we find that (i) locally, the Fisher linear discriminant direction sharply distinguishes regions of correct vs incorrect blackness correlation, and (ii) several interactions have consistently strong effects in most of the parameter space, namely, c_v, c_u, c_1, and c_4.

Our analyses indicate that blackness correlation does not constrain the sign of c_5 as (i) this parameter does not significantly contribute to the Fisher linear discriminant direction $\mathbf{v}_{\mathrm{FLD}}$ [Fig. 6(d), lower panel] and (ii) parameter sets with negative and positive c_5 exhibit good blackness correlation [Fig. 6(d), upper left-hand panel] in addition to good nearest-neighbor statistics. However, we find that blackness correlation direction may favor negative values of c_5 if the interaction network is symmetrized by constraining $c_1 = c_4$, $c_3 = c_6$, and $c_u = c_v$, i.e., when assuming that production, decay, and cross-interaction are not significantly different between melanophores and xanthophores. One could argue that this assumption is justified by the fundamental difference of interpretation between short-range and long-range interactions between chromatophores. Hence, we scanned through 96 000 000 sets of parameter values randomly drawn from a uniform distribution in the box,

$$\begin{aligned} c_1, c_2, c_8 &\in [-0.25, 0], \qquad c_4 = c_1, \\ c_7, c_u, c_w &\in [0, 0.25], \qquad c_v = c_u, \\ c_3, c_9 &\in [0, 1], \qquad c_6 = c_3, \\ c_5 &\in [-0.25, 0.25], \end{aligned} \tag{C4}$$

while diffusion and geometric parameters are kept at their usual values. The density of this sampling is equivalent to a grid scan with increment ≈ 0.048 in all the varied parameters. Among the randomly drawn parameter sets, 775 give natural nearest-neighbor statistics, among which 62 give correct blackness correlation direction (Supplemental Material, Fig. S20A [34]). An example of a set of parameter values giving good patterns and correct correlation is shown in Supplemental Material Fig. S20B [34]. We can therefore say that the "symmetric" hypothesis cannot be rejected. Projections of the data suggest that parameters $c_{1,4}$, $c_{3,6}$, c_5, and $c_{u,v}$ may influence the correlation direction (Supplemental Material, Fig. S20C [34]). Again, to determine which parameters influence the most the correlation direction, we computed $\mathbf{v}_{\mathrm{FLD}}$ best separating the two groups and found that the most significantly nonzero components are given by $c_{1,4}$, $c_{3,6}$, and $c_{u,v}$ (lower panel of Supplemental Material Fig. S20D [34]). These correspond to the following changes in the interaction network of the model (Supplemental Material, Fig. S20E [34]): (i) decrease of the effective mutual inhibition $c_{1,4}$ of the chromatophore factors u and v, (ii) increase of the effective production $c_{3,6}$ of the chromatophore factors u and v, and (iii) increase of the effective decay $c_{u,v}$ of the chromatophore factors u and v (found to give the most important contribution to the linear discriminant direction).

It is also seen that in the scanned parameter region, the subregion with $c_5 < 0$ is statistically favored for giving patterns with both natural nearest-neighbor statistics and correct blackness correlation direction (Supplemental Material, Figs. S20C and S20D [34]). Indeed, in the subregion $c_5 < 0$, we found 43 sets of parameter values with good correlation out of 173 with good neighbor statistics (i.e., about 25%), whereas in the subregion $c_5 \geq 0$, we found only 19 parameters with correct blackness correlation direction ("ok") out of 540 with good neighborhood statistics (i.e., about 3.5%). Hence, using Bayes's formula,

$$p(c_5 < 0|\mathrm{ok}) = \frac{p(\mathrm{ok}|c_5 < 0)p(c_5 < 0)}{p(\mathrm{ok}|c_5 < 0)p(c_5 < 0) + p(\mathrm{ok}|c_5 \geq 0)p(c_5 \geq 0)}, \tag{C5}$$

with uniform prior on the sign of c_5, we evaluate that the probability $p(c_5 < 0|\mathrm{ok})$ of c_5 to be negative is 85% (vs 65% for the unconstrained asymmetrical model) when considering only the information of the natural nearest-neighbor statistics and the correct blackness correlation direction for green scales. So, in this symmetric model, there is a slight preference for $c_5 < 0$. We note that this argument of preference for a negative c_5 in the symmetrical model is contingent on the sampling of the parameter space (which was here uniform and restricted inside the box given above).

[1] A. M. Turing, *The chemical basis of morphogenesis*, Phil. Trans. R. Soc. B **237**, 37 (1952).

[2] M. Cross and H. Greenside, *Pattern Formation and Dynamics in Nonequilibrium Systems* (Cambridge University Press, Cambridge, England, 2009).

[3] A. Gierer and H. Meinhardt, *A theory of biological pattern formation*, Kybernetik **12**, 30 (1972).

[4] M. C. Cross and P. C. Hohenberg, *Pattern formation outside of equilibrium*, Rev. Mod. Phys. **65**, 851 (1993).

[5] J. D. Murray, *Mathematical Biology II: Spatial Models and Biomedical Applications*, Interdisciplinary Applied Mathematics, Vol. 18 (Springer, New York, 2003).

[6] S. Kondo and T. Miura, *Reaction-diffusion model as a framework for understanding biological pattern formation*, Science **329**, 1616 (2010).

[7] F. Schweisguth and F. Corson, *Self-organization in pattern formation*, Dev. Cell **49**, 659 (2019).

[8] J. B. A. Green and J. Sharpe, *Positional information and reaction-diffusion: Two big ideas in developmental biology combine*, Development **142**, 1203 (2015).

[9] L. Wolpert, *Positional information and the spatial pattern of cellular differentiation*, J. Theor. Biol. **25**, 1 (1969).

[10] L. Wolpert, *Positional Information and Pattern Formation* (Academic Press, New York, 1971), Chap. 6, pp. 183–224.

[11] M. Akam, *Making stripes inelegantly*, Nature (London) **341**, 282 (1989).

[12] J. T. Bagnara and J. Matsumoto, *The Pigmentary System: Physiology and Pathophysiology* (John Wiley & Sons, New York, 2008), p. 11.

[13] T. Kuriyama, K. Miyaji, M. Sugimoto, and M. Hasegawa, *Ultrastructure of the dermal chromatophores in a lizard (Scincidae: Plestiodon latiscutatus) with conspicuous body and tail coloration*, Zoological science **23**, 793 (2006).

[14] S. Kinoshita, S. Yoshioka, and J. Miyazaki, *Physics of structural colors*, Rep. Prog. Phys. **71**, 076401 (2008).

[15] S. V. Saenko, J. Teyssier, D. van der Marel, and M. C. Milinkovitch, *Precise colocalization of interacting structural and pigmentary elements generates extensive color pattern variation in phelsumalizards*, BMC Biol. **11**, 105 (2013).

[16] J. Teyssier, S. V. Saenko, D. van der Marel, and M. C. Milinkovitch, *Photonic crystals cause active colour change in chameleons*, Nat. Commun. **6**, 6368 (2015).

[17] A. Nakamasu, G. Takahashi, A. Kanbe, and S. Kondo, *Interactions between zebrafish pigment cells responsible for the generation of Turing patterns*, Proc. Natl. Acad. Sci. U.S.A. **106**, 8429 (2009).

[18] H. G. Frohnhöfer, J. Krauss, H.-M. Maischein, and C. Nüsslein-Volhard, *Iridophores and their interactions with other chromatophores are required for stripe formation in zebrafish*, Development **140**, 2997 (2013).

[19] H. Hamada, M. Watanabe, H. E. Lau, T. Nishida, T. Hasegawa, D. M. Parichy, and S. Kondo, *Involvement of Delta/Notch signaling in zebrafish adult pigment stripe patterning*, Development **141**, 318 (2014).

[20] A. P. Singh, U. Schach, and C. Nüsslein-Volhard, *Proliferation, dispersal and patterned aggregation of iridophores in the skin prefigure striped colouration of zebrafish*, Nat. Cell Biol. **16**, 604 (2014).

[21] D. S. Eom and D. M. Parichy, *A macrophage relay for long-distance signaling during postembryonic tissue remodeling*, Science **355**, 1317 (2017).

[22] L. B. Patterson and D. M. Parichy, *Zebrafish pigment pattern formation: Insights into the development and evolution of adult form*, Annu. Rev. Genet. **53**, 505 (2019).

[23] M. Inaba, H. Yamanaka, and S. Kondo, *Pigment pattern formation by contact-dependent depolarization*, Science **335**, 677 (2012).

[24] L. Manukyan, S. A. Montandon, A. Fofonjka, S. Smirnov, and M. C. Milinkovitch, *A living mesoscopic cellular automaton made of skin scales*, Nature (London) **544**, 173 (2017).

[25] A. Fofonjka and M. C. Milinkovitch, *Reaction-diffusion in a growing 3D domain of skin scales generates a discrete cellular automaton*, Nat. Commun. **12**, 2433 (2021).

[26] J. von Neumann, *Cerebral Mechanisms in Behavior: The Hixon Symposium* (Wiley, New York, 1951), p. 228.

[27] J. Von Neumann and A. W. Burks, *Theory of Self-Reproducing Automata*, 1st ed. (University of Illinois Press, Urbana and London, 1966).

[28] S. Wolfram, *Computation theory of cellular automata*, Commun. Math. Phys. **96**, 15 (1984).

[29] S. Wolfram *et al.*, *A New Kind of Science*, Vol. 5 (Wolfram Media, Champaign, IL, 2002).

[30] S. Zakany, S. Smirnov, and M. C. Milinkovitch, *Lizard skin patterns and the Ising model*, Phys. Rev. Lett. **128**, 048102 (2022).

[31] W. Lenz, *Beitrag zum Verständnis der magnetischen Erscheinungen in festen Körpern*, Z. Phys. **21**, 613 (1920).

[32] E. Ising, *Beitrag zur theorie des ferromagnetismus*, Z. Phys. **31**, 253 (1925).

[33] E. Jahanbakhsh and M. C. Milinkovitch, *Modeling convergent scale-by-scale skin color patterning in multiple species of lizards*, Curr. Biol. **32**, 5069 (2022).

[34] See Supplemental Material at http://link.aps.org/supplemental/10.1103/PhysRevX.13.041011 for the Supplemental Table and Supplemental Figures.

[35] A. F. Martins, M. Bessant, L. Manukyan, and M. C. Milinkovitch, *R2OBBIE-3D, a fast robotic high-resolution system for quantitative phenotyping of surface geometry and colour-texture*, PLoS One **10**, 1 (2015).
[36] P. Gray and S. Scott, *Autocatalytic reactions in the isothermal, continuous stirred tank reactor: Oscillations and instabilities in the system* $A + 2B \rightarrow 3B$; $B \rightarrow C$, Chem. Eng. Sci. **39**, 1087 (1984).
[37] J. E. Pearson, *Complex patterns in a simple system*, Science **261**, 189 (1993).
[38] S. M. Allen and J. W. Cahn, *A microscopic theory for antiphase boundary motion and its application to antiphase domain coarsening*, Acta Metall. **27**, 1085 (1979).
[39] The effective dRD diffusion coefficients were not varied to avoid regimes where the dRD becomes a poor description of the underlying system.
[40] P. Mahalwar, B. Walderich, A. P. Singh, and C. Nüsslein-Volhard, *Local reorganization of xanthophores fine-tunes and colors the striped pattern of zebrafish.*, Science **345**, 1362 (2014).
[41] A. P. Singh and C. Nüsslein-Volhard, *Zebrafish stripes as a model for vertebrate colour pattern formation*, Curr. Biol. **25**, R81 (2015).
[42] M. Watanabe and S. Kondo, *Comment on "Local reorganization of xanthophores fine-tunes and colors the striped pattern of zebrafish,"* Science **348**, 297 (2015).
[43] A. Volkening and B. Sandstede, *Iridophores as a source of robustness in zebrafish stripes and variability in Danio patterns*, Nat. Commun. **9**, 3231 (2018).
[44] X. Trepat and E. Sahai, *Mesoscale physical principles of collective cell organization*, Nat. Phys. **14**, 671 (2018).
[45] M. C. Milinkovitch, *Emergence of self-organizational patterning at the mesoscopic scale*, Dev. Cell **56**, 719 (2021).
[46] W. Härdle and L. Simar, *Applied Multivariate Statistical Analysis* (Springer, Berlin, 2015).
[47] Y. Hochberg and A. C. Tamhane, *Multiple Comparison Procedures* (Wiley, New York, 2009).
[48] S. A. Montandon, A. C. Tzika, A. F. Martins, B. Chopard, and M. C. Milinkovitch, *Two waves of anisotropic growth generate enlarged follicles in the spiny mouse*, EvoDevo **5**, 33 (2014).
[49] For the parameter scan performed in Sec. IV, around 80% of the parameter sets found to give nontrivial spatial patterns were in this case.
[50] H. Hotelling, *The generalization of student's ratio*, Ann. Math. Stat. **2**, 360 (1931).